The Company of Biologists

RESEARCH ARTICLE   **SPECIAL ISSUE: CELL BIOLOGY OF LIPIDS**

The endoplasmic reticulum–plasma membrane tethering protein TMEM24 is a regulator of cellular Ca^{2+} homeostasis

Beichen Xie[1], Styliani Panagiotou[1], Jing Cen[1], Patrick Gilon[2], Peter Bergsten[1] and Olof Idevall-Hagren[1,*]

ABSTRACT

Endoplasmic reticulum (ER)–plasma membrane (PM) contacts are sites of lipid exchange and Ca^{2+} transport, and both lipid transport proteins and Ca^{2+} channels specifically accumulate at these locations. In pancreatic β-cells, both lipid and Ca^{2+} signaling are essential for insulin secretion. The recently characterized lipid transfer protein TMEM24 (also known as C2CD2L) dynamically localizes to ER–PM contact sites and provides phosphatidylinositol, a precursor of phosphatidylinositol-4-phosphate [PI(4)P] and phosphatidylinositol 4,5-bisphosphate [PI(4,5)P$_2$], to the PM. β-cells lacking TMEM24 exhibit markedly suppressed glucose-induced Ca^{2+} oscillations and insulin secretion, but the underlying mechanism is not known. We now show that TMEM24 only weakly interacts with the PM, and dissociates in response to both diacylglycerol and nanomolar elevations of cytosolic Ca^{2+}. Loss of TMEM24 results in hyper-accumulation of Ca^{2+} in the ER and in excess Ca^{2+} entry into mitochondria, with resulting impairment in glucose-stimulated ATP production.

KEY WORDS: Membrane contact sites, Ca^{2+}, Insulin secretion, Phosphoinositides, Mitochondria

INTRODUCTION

Lipid exchange between the endoplasmic reticulum (ER) and the plasma membrane (PM) is facilitated by lipid transport proteins that are concentrated to, and participate in the formation of, ER–PM contact sites. These junctions are also important sites for cellular Ca^{2+} homeostasis, and the lipid transport is often coupled to changes in the cytosolic Ca^{2+} concentration (Balla, 2018; Chung et al., 2017; Saheki and De Camilli, 2017). The changes in membrane lipid concentrations occurring as a consequence of lipid transport may also influence Ca^{2+} influx or extrusion through modulation of Ca^{2+} channel activity or clustering (Johnson et al., 2018; Suh et al., 2010; Sun et al., 2019; Xie et al., 2016). TMEM24 is a recently characterized lipid transport protein that localizes to ER–PM contacts where it, through an N-terminal synaptotagmin-like mitochondrial-lipid-binding (SMP) domain, provides the PM with phosphatidylinositol, the precursor of the signaling lipids phosphatidylinositol-4-phosphate [PI(4)P] and phosphatidylinositol

4,5-bisphosphate [PI(4,5)P$_2$] (Lees et al., 2017; Sun et al., 2019). It binds negatively charged lipids in the PM via a C-terminal polybasic region, and neutralization of positively charged amino acids in this region by protein kinase C (PKC)-dependent phosphorylation results in TMEM24 dissociation from the PM. TMEM24 is also equipped with a C2 domain, which, however, seems dispensable for both PM binding and lipid transport. The spatial regulation of TMEM24 activity differs from other SMP- and C2-domain proteins, such as the extended synaptotagmins, whose interaction with the PM and lipid transport are instead triggered by Ca^{2+} elevation (Bian et al., 2018; Giordano et al., 2013; Idevall-Hagren et al., 2015).

Pancreatic β-cells are secretory cells that produce insulin and release this hormone to the circulation in response to elevated blood glucose levels. The mechanism controlling insulin secretion is well-characterized and involves glucose uptake and metabolism, resulting in an elevated ATP/ADP ratio which, in turn, closes ATP-sensitive K$^+$ (K$_{ATP}$)-channels, causing membrane depolarization, opening of voltage-dependent Ca^{2+} channels, Ca^{2+} influx and the fusion of insulin-containing granules with the PM (Rorsman and Ashcroft, 2018). Ca^{2+} is the most important trigger of insulin secretion, but the response can also be modulated by many factors, including lipids and lipid-derived signaling molecules. Phosphoinositides in particular have been shown to regulate insulin secretion at several stages, including membrane depolarization, Ca^{2+} influx and granule docking and release (Wuttke, 2015). The phosphoinositide PI(4,5)P$_2$ also serves as a precursor of inositol 1,4,5-trisphosphate (IP3), which triggers Ca^{2+} release from the ER and may contribute to insulin granule exocytosis, and diacylglycerol (DAG), which together with Ca^{2+} amplifies secretion by stimulating the PKC activity (Wuttke et al., 2013, 2016). Lipid transport at ER–PM contact sites is important for the normal function of insulin-secreting β-cells. DAG transport by E-Syt1 was recently found to provide negative feedback on insulin secretion after being recruited to sites of Ca^{2+} influx, where it locally clears the PM of the pro-secretory lipid (Xie et al., 2019). β-cells with reduced E-Syt1 expression thus exhibit increased accumulation of PM DAG and excess insulin secretion in response to glucose. E-Syt1 occupies the same contact sites as TMEM24. However, their presence at these contacts does not overlap in time due to their opposite dependence of PM binding on the prevailing Ca^{2+} concentration (Xie et al., 2019). Interestingly, TMEM24 was recently found to be indispensable for glucose-stimulated insulin secretion (Lees et al., 2017; Pottekat et al., 2013). The complete loss of insulin secretion in clonal TMEM24-knockout (KO) β-cells is likely caused by an effect on β-cell Ca^{2+} homeostasis. β-cells lacking TMEM24 thus exhibit markedly suppressed glucose-induced Ca^{2+} oscillations, but the mechanism behind this is not clear (Lees et al., 2017). One possibility is that TMEM24 is necessary for maintaining the PM PI(4,5)P$_2$ level, which is required for ion channel gating during stimulation, although the global PI(4,5)P$_2$ levels are unaltered in TMEM24 KO cells (Lees et al.,

[1]Department of Medical Cell Biology, Uppsala University, BMC Box 571, 75123 Uppsala, Sweden. [2]Pole of Endocrinology, Diabetes and Nutrition (EDIN), Institute of Experimental and Clinical Research (IREC), Université Catholique de Louvain, Avenue Hippocrate 55, B1.55.06 B-1200 Brussels, Belgium.

*Author for correspondence (olof.idevall@mcb.uu.se)

O.I., 0000-0002-0241-6304

2017). The dynamics of TMEM24 in glucose-stimulated β-cells is also difficult to reconcile with a role as a positive regulator of insulin secretion, since it is spatially separated from this process during glucose stimulation. Clarification of the role of TMEM24 in the regulation of insulin secretion is therefore required.

We now show that the subcellular distribution of TMEM24 is highly dynamic and influenced by both Ca^{2+} and PM DAG. In contrast to previous studies, we do not find an absolute requirement of TMEM24 for normal Ca^{2+}-triggered insulin secretion. Instead, we show that TMEM24 supports sustained insulin secretion by regulating ER and mitochondrial Ca^{2+} handling and mitochondrial energy production.

RESULTS
TMEM24 PM binding is controlled by DAG and Ca^{2+}
To better understand the role of TMEM24 in the regulation of β-cell function, we investigated conditions that promote TMEM24 dissociation from the PM. Elevation of the glucose concentration from 3 to 20 mM in clonal MIN6 β-cells loaded with the Ca^{2+} indicator Cal590 resulted in regular cytosolic Ca^{2+} oscillations with elevations mirrored by synchronized TMEM24–GFP dissociations, seen as reductions in PM-proximal fluorescence by total internal reflection fluorescence (TIRF) microscopy (Fig. 1A–C), similar to what has previously been reported (Lees et al., 2017). Direct depolarization with 30 mM KCl also caused dissociation of TMEM24 from the PM, consistent with voltage-dependent Ca^{2+} influx being the trigger for dissociation (Fig. 1B–D). Similar TMEM24 dissociation was also seen in response to carbachol, which activates phospholipase C and triggers IP3-mediated release of Ca^{2+} from the ER (Fig. 1B,C). Passive depletion of ER Ca^{2+} using the sarcoendoplasmic reticulum (SR) Ca^{2+} transport ATPase (SERCA) inhibitor cyclopiazonic acid (CPA) also triggered TMEM24 dissociation, although less prominently than in response to carbachol (Fig. 1B,C). Glucose-induced TMEM24 dissociation has previously been shown to depend on PKC-mediated phosphorylation of C-terminal residues in the molecule (Lees et al., 2017). Although Ca^{2+} is a potent activator of PKC, some isoforms also require DAG. To determine to what extent DAG is involved in the spatial control of TMEM24, we stimulated MIN6 cells with 1 μM of the DAG analog phorbol 12-myristate 13-acetate (PMA). This resulted in an immediate dissociation of TMEM24 from the PM without apparent change in the cytosolic Ca^{2+} concentration (Fig. 1B,C; Fig. S1A,B). To further uncouple DAG formation from Ca^{2+} changes, we first exposed cells to CPA to deplete ER Ca^{2+} stores, followed by addition of carbachol to activate PLC and increase PM DAG. CPA caused an increase in cytosolic Ca^{2+} and a slight dissociation of GFP–TMEM24 from the PM. The subsequent addition of carbachol resulted in a pronounced dissociation of TMEM24 that occurred in the absence of noticeable changes in cytosolic Ca^{2+} concentration (Fig. S1C–E). These results indicate that TMEM24 is spatially controlled by both Ca^{2+} and DAG. We also noticed that whereas carbachol caused a homogenous dissociation of TMEM24 from the PM (Fig. 1E, right panels), the dissociation in response to direct depolarization with KCl was instead incomplete, more heterogenous and differed between sub-regions of the PM within the same cell (Fig. 1E, left panels). This pattern resembles that of the DAG biosensor GFP–C1aC1b$_{PKC}$, which reports DAG formation after autocrine activation of purinergic P2Y1 receptors by ATP co-secreted with insulin from the cells (Wuttke et al., 2013; Fig. S1F,G). Because of the close interplay between DAG and Ca^{2+}, we determined the effect of known Ca^{2+} concentrations on TMEM24–mCherry PM

binding in α-toxin-permeabilized MIN6 cells in which changes in Ca^{2+} could easily be uncoupled from those in DAG. We found that dissociation of TMEM24 occurred with an EC_{50} of 358±70 nM (mean±s.e.m.; $n=13$) and was maximal at 30 μM (Fig. 1F,G). As mentioned above, addition of 1 μM PMA caused pronounced dissociation of TMEM24 from the PM and a subsequent stepwise increase in the Ca^{2+} concentration had little effect on TMEM24 PM binding (Fig. S1H,I). For comparison, the PM binding of E-Syt1–mCherry, another Ca^{2+}-dependent ER–PM contact protein, was triggered at 1 μM Ca^{2+} and was maximal at 10 μM Ca^{2+} (EC_{50} 1.99±0.51 μM, $n=6$) (Fig. 1G). When comparing the PM fluorescence intensity of TMEM24–mCherry in intact cells and following permeabilization in a Ca^{2+}-free buffer, we found that removal of Ca^{2+} promoted further association of TMEM24 with the PM (13±5% increase in PM TMEM24–mCherry fluorescence, $n=22$, $P<0.01$) (Fig. 1H) while the opposite was observed for GFP–E-Syt1 (29±4% drop in PM fluorescence, $n=31$). These results indicate that TMEM24 PM binding might be partially reduced already at resting Ca^{2+} concentrations. Fluorescence recovery after photobleaching (FRAP) analysis revealed that TMEM24–GFP, although enriched at ER–PM contacts, exhibited pronounced dynamics with a large proportion belonging to a mobile fraction (Fig. 1I). Taken together, these results show that the association of TMEM24 with the PM is regulated by both DAG and Ca^{2+}, and that dissociation can be triggered by modest nanomolar Ca^{2+} concentrations, resulting in relatively weak interactions between TMEM24 and the PM.

Regulation of glucose-induced Ca^{2+} signaling and insulin secretion by TMEM24
TMEM24 has previously been reported to be required for glucose-stimulated Ca^{2+} influx and insulin release, although the mechanisms are unclear (Lees et al., 2017). To examine its role in more detail, we reduced TMEM24 expression in MIN6 cells by siRNA-mediated transient knockdown (KD), which resulted in a 61.2±6.3% (mean±s.e.m.; $n=4$, $P<0.01$) reduction in TMEM24 expression as assessed by western blotting (86.7±5.2% reduction as assessed by qRT-PCR; data not shown) (Fig. 2A). We next determined the impact of reduced TMEM24 expression on Ca^{2+} handling using the fluorescent Ca^{2+} indicator Cal520. In control cells, elevation of the glucose concentration from 3 to 20 mM resulted in rapid lowering of the cytosolic Ca^{2+} concentration ($-17.1±0.9\%$, $n=148$) due to ATP-driven sequestration of the ion into the ER (Roe et al., 1994), followed after 2.8±0.09 min by a pronounced Ca^{2+} increase and sustained elevation (Fig. 2B–E). Most cells showed slow regular Ca^{2+} oscillations in the continued presence of 20 mM glucose, whereas a smaller number showed more irregular responses (Fig. 2B). In TMEM24 KD cells, the initial Ca^{2+} lowering in response to 20 mM glucose was less pronounced ($-12.4±0.8\%$, $n=137$, $P=0.0016$ for comparison to control) and was followed after 3.31±0.11 min ($n=141$, $P=0.003$ for comparison to control) by a sustained rise of Ca^{2+} with regular oscillations (Fig. 2B,C,E). The time-average increase in Ca^{2+} was slightly higher in TMEM24 KD cells compared to controls (Fig. 2D). Overexpression of TMEM24 resulted in an exaggerated initial lowering of the cytosolic Ca^{2+} concentration in response to glucose and a slightly increased sustained Ca^{2+} response when compared to non-transfected control cells (Fig. 2C–E). To ascertain that the relatively mild effect on Ca^{2+} handling in TMEM24 KD cells was not due to remaining low TMEM24 expression, we generated TMEM24 KO MIN6 cell lines using CRISPR/Cas9 (Fig. 2F). Both control and TMEM24 KO cells exhibited glucose-induced oscillations in the cytosolic Ca^{2+}
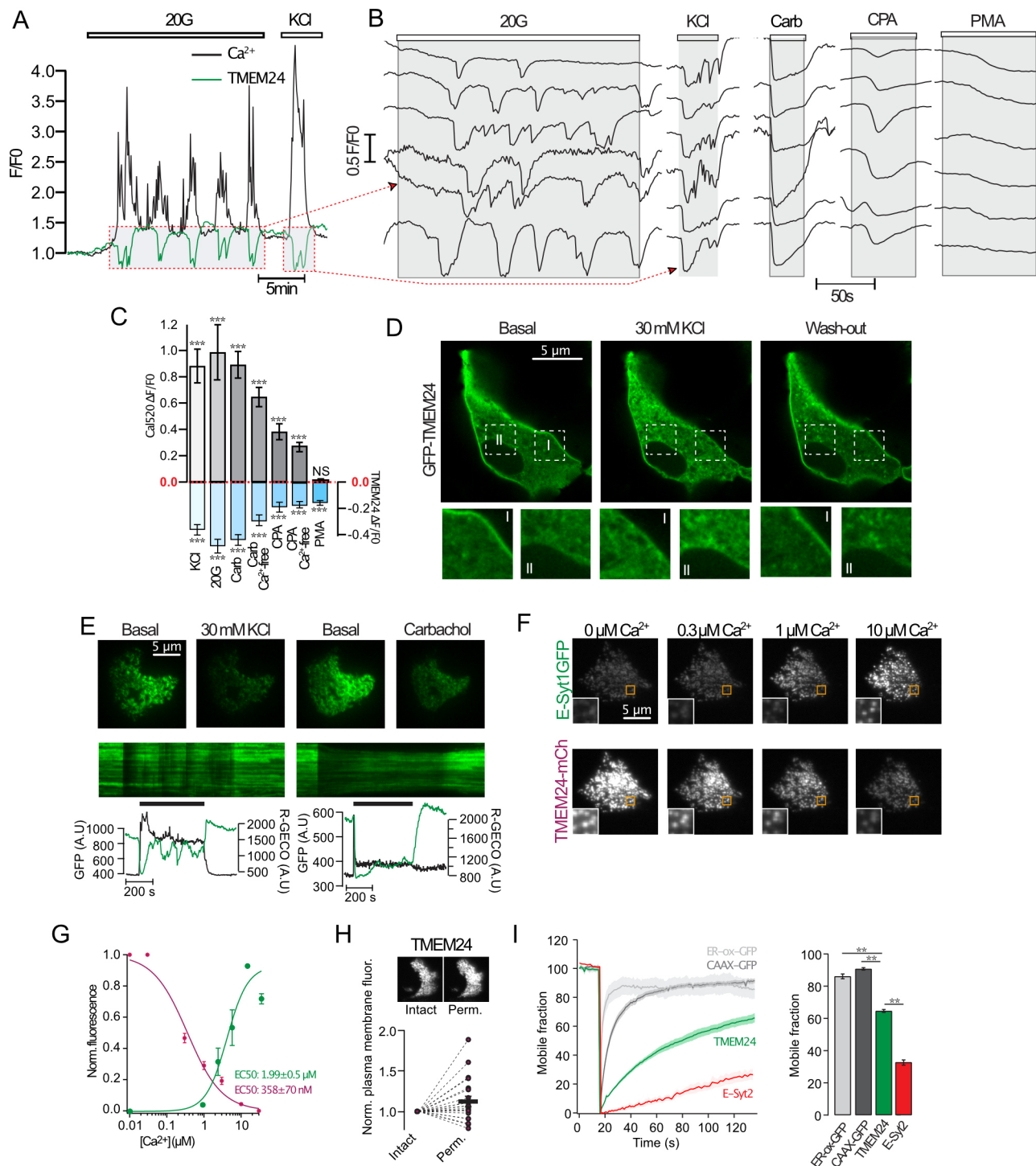
Fig. 1. See next page for legend.

concentration, although the time-averaged Ca^{2+} increase was reduced by $21\pm2\%$ ($P=1.47\times10^{-9}$) in the TMEM24 KO cells (Fig. 2G–I). Similar to what was seen in TMEM24 KD, the KO cell line also exhibited strongly suppressed initial Ca^{2+} lowering in response to glucose (Fig. 2J,K). Both TMEM24 KD and TMEM24 KO cells exhibited Ca^{2+} responses to glucose that contained a component of rapid Ca^{2+} transients superimposed on top of the regular, slow Ca^{2+} oscillations (Fig. 2B,G).

Given the relatively small effect of TMEM24 KD or KO on glucose-induced Ca^{2+} influx observed here, we decided to reinvestigate the previously proposed fundamental role of TMEM24 in insulin secretion (Lees et al., 2017; Pottekat et al., 2013). Using insulin ELISA, we found that basal secretion at 3 mM glucose and that stimulated by 20 mM glucose were similar in control and TMEM24 KD and KO cells (Fig. 2N). There were also no differences in insulin content between control cells and TMEM24 KD or KO cells (Fig. 2L,M). To investigate the secretion kinetics under conditions more similar to those of primary β-cells within islets of Langerhans, we allowed wild-type and TMEM24 KO cells to aggregate into islet-like cell clusters

Fig. 1. TMEM24 PM binding is controlled by DAG and Ca^{2+}. (A) TIRF microscopy recording of Ca^{2+} indicator Cal590 (black) and TMEM24–EGFP (green) fluorescence from a single MIN6 cell stimulated with 20 mM glucose (20G) and 30 mM KCl. (B) Representative TIRF microscopy recordings from TMEM24–EGFP-expressing MIN6 cells in response to 20 mM glucose, 30 mM KCl, 100 µM carbachol, 100 µM CPA and 1 µM PMA. (C) Quantification of Ca^{2+} increases (gray) and the corresponding magnitude of TMEM24–EGFP dissociation from the PM (blue), n=20 cells for each group (N=3). ***P<0.001; NS, not significant for comparison to 0 (unpaired two-tailed Student's t-test). (D) Confocal microscopy images of a MIN6 cell expressing TMEM24–EGFP. Images were taken before, during and 30 s after depolarization. Content within the dashed boxes is magnified below. (E) TIRF microscopy images of two MIN6 cells expressing TMEM24–EGFP. Pictures to the left show cells before and 30 s after the addition of 30 mM KCl and pictures to the right show cells before and 30 s after addition of 100 µM carbachol. Shown below are kymographs of TMEM24–EGFP fluorescence from lines drawn across each a cell and TIRF microscopy recordings from the same cell (black trace, Cal590 fluorescence; green trace, TMEM24–EGFP fluorescence). Black bars above kymographs show time when KCl (left) or carbachol (right) is present. AU, arbitrary units. (F) TIRF microscopy images of a MIN6 cell expressing E-Syt1–GFP (top) or TMEM24–mCherry (bottom) following α-toxin permeabilization and exposure to the indicated Ca^{2+} buffers. Magnified views of the area within the orange box are shown in the inset. (G) Dose–response curves of Ca^{2+} induced TMEM24-mCherry (magenta) and E-Syt1–GFP (green) fluorescence changes in α-toxin-permeabilized MIN6 cells (n=42; N=5). Data points were fitted to a sigmoidal curve using the Hill equation. (H) TIRF microscopy images of a MIN6 cell expressing TMEM24–mCherry before (intact) and after α-toxin permeabilization (perm). Quantifications below show the PM fluorescence change that occurred following α-toxin permeabilization in a Ca^{2+}-deficient buffer (n=22; N=6). (I) TIRF microscopy recordings of ER–oxGFP (ER luminal protein; light gray), GFP–CAAX (prenylated protein anchored in the PM; dark gray), TMEM24–EGFP (green) and E-Syt2–GFP (red) fluorescence recovery after photobleaching (FRAP). Bar graph to the right shows the mobile fraction of each fluorescently tagged protein (n=12 cells per condition; N=4). All data are presented as mean±s.e.m., **P<0.01, ***P<0.001 (Kruskal–Wallis one-way ANOVA and Mann–Whitney U-test).

(pseudo-islets). This preparation enhances the secretory capacity of the MIN6 cells by enabling electrical coupling and upregulating glucose-sensing and metabolic pathways (Chowdhury et al., 2013). Perifusion of wild-type MIN6 pseudo-islets during a step-increase in glucose concentration from 3 mM to 20 mM resulted in an initial peak of insulin secretion (first phase), followed by sustained secretion at a level much above basal secretion (second phase). TMEM24 KO pseudo-islets displayed a similar biphasic secretion pattern but the second phase of secretion was less pronounced than in wild-type cells (Fig. 2O,P). Taken together, these results question the previously reported absolute requirement of TMEM24 for glucose-stimulated insulin secretion, and instead indicate that TMEM24 plays a regulatory role during sustained insulin secretion.

TMEM24 controls ER Ca^{2+} homeostasis
Since we observed a slightly impaired Ca^{2+} response to glucose in TMEM24 KO cells, we tested to what extent Ca^{2+} influx in response to direct depolarization was affected by the loss of TMEM24. The resting cytosolic Ca^{2+} concentration was similar in wild-type and TMEM24 KO cells. Depolarization with 30 mM KCl resulted in an immediate rise of cytosolic Ca^{2+} that averaged 361±5 nM (n=298) in wild-type cells. This response was increased to 441±8 nM (mean±s.e.m.; n=317, P=3.12×10^{-16}) in TMEM24 KO cells (Fig. 3A,B). Consistent with more Ca^{2+} entering the cells in response to depolarization, we also found that insulin secretion in response to acute depolarization was increased by 60% in TMEM24 KO cells (n=12, P=0.019) (Fig. 3G). Similar results were obtained

from cells where TMEM24 expression had instead been reduced by siRNA (Fig. 3D–F,H). Several observations made in TMEM24 KO cells, such as lack of initial Ca^{2+}-lowering effect of glucose and the appearance of irregular Ca^{2+} spikes, pointed to potential changes in the ability of the ER to sequester and mobilize Ca^{2+}. To test this more directly, we mobilized Ca^{2+} from the ER by the SERCA inhibitor CPA in the absence of extracellular Ca^{2+} while measuring changes in the cytosolic Ca^{2+} concentration. The addition of CPA resulted in a 32±1 nM (n=298) increase in the cytosolic Ca^{2+} concentration, reflecting the release of Ca^{2+} from the ER. This release was increased to 48±2 nM (n=306, P=9.8×10^{-12}) in TMEM24 KO cells (Fig. 3I,J). The addition of 10 mM Ca^{2+} to the extracellular buffer triggered store-operated Ca^{2+} entry, which was not different in the two cell lines (Fig. 3K). Similar results were obtained in cells where TMEM24 expression was reduced by siRNA (Fig. S2) and when ER Ca^{2+}-store depletion was instead triggered by the addition of thapsigargin in the presence of extracellular Ca^{2+}. Importantly, the response in TMEM24 KO cells returned to normal upon the re-expression of wild-type TMEM24 (Fig. 3L), whereas overexpression of TMEM24 in wild-type cells resulted in reduced release of Ca^{2+} from the ER (Fig. S2). Direct measurements of ER Ca^{2+} using the FRET-based Ca^{2+} sensor D4ER confirmed that the ER of TMEM24 KO cells contained more Ca^{2+} than that of wild-type cells under resting conditions, and also that more Ca^{2+} was released from the ER following SERCA inhibition with CPA (Fig. 3M,N). We speculated that the larger rise of cytosolic Ca^{2+} in response to depolarization in TMEM24 KO cells might be due to simultaneous Ca^{2+}-induced Ca^{2+} release from the ER. To test this alternative, we performed experiments where cytosolic Ca^{2+} was measured following two brief applications of 30 mM KCl, where the second application was preceded by SERCA inhibition with thapsigargin. Consistent with previous observations (Chen et al., 2003), prevention of Ca^{2+} sequestration into the ER by SERCA inhibition resulted in a more pronounced depolarization-induced Ca^{2+} increase in wild-type cells (Fig. 3N,O). This augmentation was even more apparent in TMEM24 KO cells, and could be restored to the level of wild-type cells by the re-expression of TMEM24 (Fig. 3P,Q). These results indicate that Ca^{2+} sequestration into the ER may be a way to compensate for excess Ca^{2+} increase in TMEM24 KO cells rather than being the cause of it.

TMEM24 regulates mitochondrial Ca^{2+} handling and ATP production
Because Ca^{2+} influx, extrusion and organellar sequestration all depends on ATP generated primarily via mitochondrial metabolism, we decided to complement the Ca^{2+} imaging with direct measurement of glucose metabolism using the Seahorse XF technique. As expected from the Ca^{2+} imaging data, TMEM24 KO had little effect on the resting oxygen consumption rate (OCR) (Fig. 4A). In contrast, the accelerated OCR induced by a rise of the extracellular glucose concentration from 3 to 20 mM was markedly impaired in TMEM24 KO cells (Fig. 4B). However, neither the proton leak nor the maximal OCR was different between wild-type and TMEM24 KO cells, indicating that there was no gross impairment in overall mitochondrial function (Fig. 4C–F). This conclusion was supported by lack of apparent changes in mitochondrial morphology in TMEM24 KO cells as assessed by confocal microscopy of cells expressing mitochondria-targeted mApple (Tom20–mApple) (Fig. 4G,H). Next, we measured the mitochondrial membrane potential in wild-type and TMEM24 KO cells using the fluorescent membrane potential indicator TMRM.
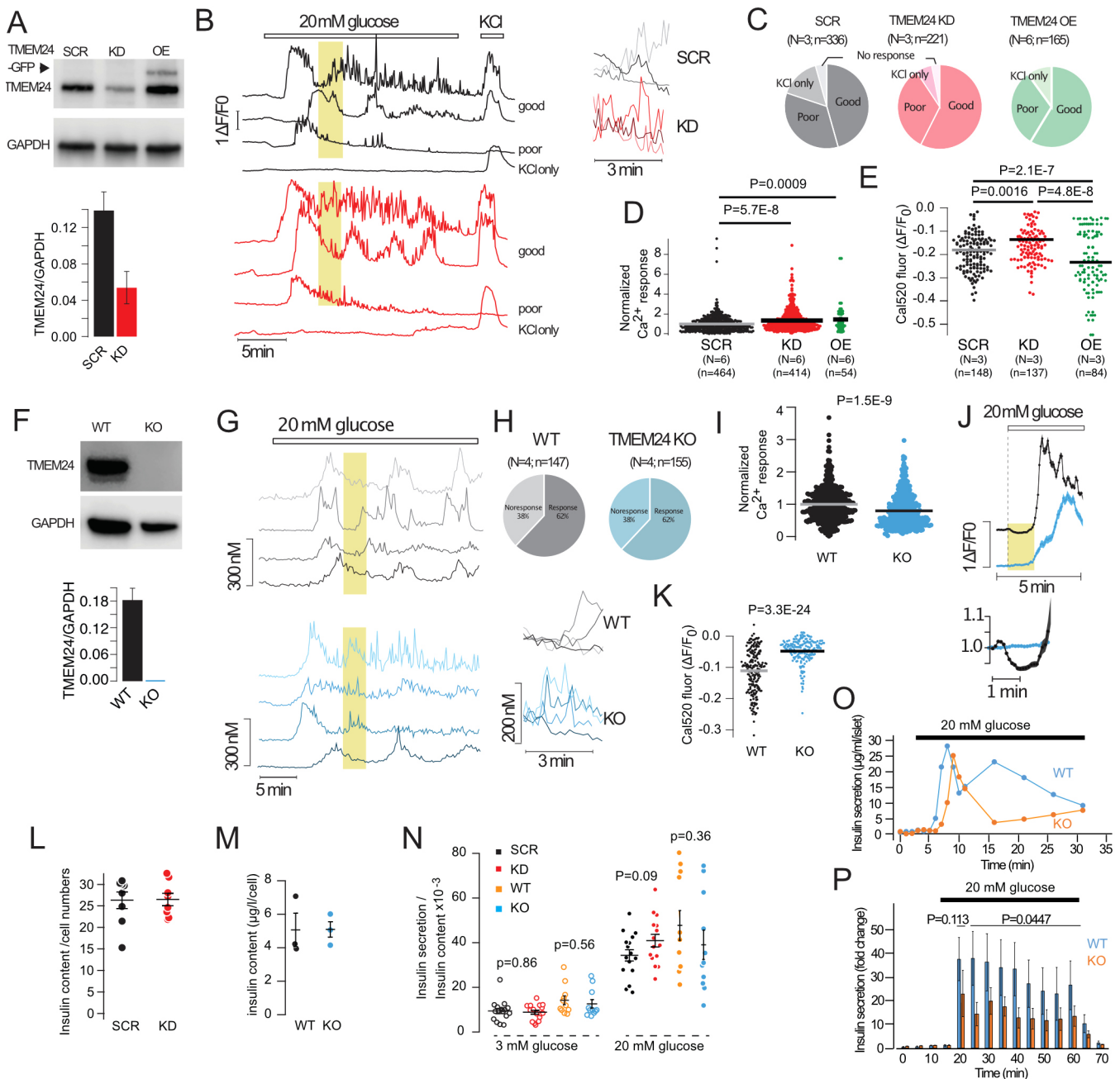
Fig. 2. See next page for legend.

Application of the uncoupler FCCP resulted in the immediate loss of TMRM fluorescence, which reflects depolarization of the inner mitochondrial membrane. This response was significantly smaller in TMEM24 KO cells, indicating that these cells already have partially depolarized mitochondria (Fig. 4I,J). The mitochondrial membrane potential not only controls ATP production by directly affecting the electron transport chain but also by regulating the amounts of Ca^{2+} that are taken up and extruded by the organelle. To determine whether TMEM24 might be involved in the regulation of mitochondrial Ca^{2+}, we measured Ca^{2+} concentration changes in response to both CPA-mediated release of Ca^{2+} from the ER and depolarization-induced Ca^{2+} influx in wild-type and TMEM24 KO cell using mitochondrially targeted LAR-GECO1.2. This low-affinity sensor has a K_d for Ca^{2+}-binding of 12 μM, and its

fluorescence is expected to increase little under normal conditions, since depolarization-induced Ca^{2+} influx typically results in Ca^{2+} concentrations in the low μM range (see e.g. Fig. 3B). Consistently, KCl depolarization of wild-type cells triggered a robust increase in the cytosolic Ca^{2+} concentration, measured with the organic dye Cal520, but had little impact on mito-LAR-GECO1.2 fluorescence in the same cells (Fig. 4K,L). In contrast, depolarization caused a pronounced increase in mito-LAR-GECO1.2 fluorescence in TMEM24 KO cells, which was reduced to the level of wild-type cells upon the re-expression of TMEM24 (Fig. 4K,L). Similar results were obtained when the Ca^{2+} increase was instead triggered by passive depletion from the ER through CPA-mediated SERCA inhibition (Fig. 4M,N). A possible explanation for these observations is that the resting mitochondrial Ca^{2+} concentration

Fig. 2. TMEM24 involvement in glucose-induced Ca²⁺ signaling and insulin secretion. (A) Western blot of lysates from MIN6 cells transfected with control (SCR) or anti-TMEM24 siRNA (KD) alone or together with TMEM24–EGFP (+TMEM24–EGFP) probed with anti-TMEM24 and GAPDH antibodies. Quantifications of densitometric measurements are shown below (n=4). (B) Representative Ca²⁺ recordings (Cal520) from control (black) and TMEM24 KD (red) MIN6 cells in response to 20 mM glucose and 30 mM KCl. The cells were divided into three groups based on the type of response: 'good', continuous response to glucose and robust response to KCl; 'poor', initial, but not sustained, response to glucose and robust response to KCl; 'KCl only', no response to glucose but robust response to KCl. The boxed yellow areas are shown to the right on an expanded time-scale. (C) Pie chart showing the distribution of Ca²⁺ responses in control (black), TMEM24 KD (red) and TMEM24-EGFP expressing (green) MIN6 cells. N and n numbers are stated above each pie chart. (D) Time-averaged Cal520 fluorescence change in response to 20 mM glucose in control (SCR, black), TMEM24 KD (KD, red) and TMEM24–EGFP-expressing (OE, green) MIN6 cells (one-way ANOVA followed by Tukey's post hoc test). (E) Quantifications of the initial, glucose-induced lowering of Cal520 fluorescence in control (SCR, black), TMEM24 KD (KD, red) and TMEM24–EGFP-expressing (OE, green) MIN6 cells (one-way ANOVA followed by Tukey's post hoc test). (F) Western blot of lysates from wild-type and TMEM24 KO MIN6 cells probed with anti-TMEM24 and GAPDH antibodies. Quantifications of densitometric measurements are shown below (n=3). (G) Representative Ca²⁺ recordings (Fura-2) from control (black) and TMEM24 KO (blue) MIN6 cells in response to 20 mM glucose. The boxed yellow areas are shown to the right on an expanded time-scale. (H) Pie chart showing the distribution of Ca²⁺ responses in wild-type (black), TMEM24 KO (blue) MIN6 cells. N and n numbers are stated above each pie chart. (I) Time-average Ca²⁺ response to 20 mM glucose in wild-type (black; n=499; N=12) and TMEM24 KO (blue; n=458; N=12) cells measured using Cal520 (unpaired two-tailed Student's t-test). (J) Initial Ca²⁺ response (Cal520) to 20 mM glucose in wild-type (black) and TMEM24 KO (blue) cells. Data presented as mean±s.e.m. for 63 (wild type) and 52 (KO) cells from one experiment. The yellow area is shown below on an expanded time scale. (K) Quantifications of the initial, glucose-induced lowering of Cal520 fluorescence in wild-type (black; n=200; N=7) and TMEM24 KO (blue; n=191; N=6) MIN6 cells (unpaired two-tailed Student's t-test). (L,M) Insulin content in control and TMEM24 KD cells (L) and in wild-type and TMEM24 KO cells (M). (N) Insulin secretion in control (black), TMEM24 KD (red), wild-type (yellow) and TMEM24 KO cells in response to 3 mM and 20 mM glucose (Kruskal–Wallis one-way analysis of variance and Mann–Whitney U-test). (O) Glucose-stimulated insulin secretion from wild-type (yellow) and TMEM24 KO (blue) MIN6 pseudo-islets exposed to a step increase on glucose concentration from 3 mM to 20 mM. Traces show secretion from one experiment. (P) Glucose-stimulated insulin secretion from wild-type (yellow) and TMEM24 KO (blue) MIN6 pseudo-islets during perifusion with the indicated glucose-containing buffer. Data from five independent experiments (Mann–Whitney U-test). WT, wild type. All data are presented as mean±s.e.m. or with mean highlighted.

is higher in TMEM24 KO cells, thus bringing the concentration into a range better suited for detection with the low-affinity sensor. Consistent with this hypothesis, we observed higher resting mito-LAR-GECO1.2 fluorescence in TMEM24 KO cells compared to wild-type cells (Fig. 4O).

We next asked how an ER-localized protein that primarily engages in lipid transport at ER–PM contact sites could impact mitochondrial function. One possibility is that TMEM24 can function at other membrane contact sites. As we show here, a large part of the PM-bound pool of TMEM24 is dynamic even under resting conditions and could therefore participate in reactions at other cellular membranes, such as those of mitochondria. To test this alternative, we expressed GFP-tagged TMEM24 together with mitochondrially localized Tom20–mApple in wild-type MIN6 cells. Using confocal microscopy, we observe enrichment of TMEM24–GFP fluorescence at mitochondria following KCl-induced Ca²⁺ increases that was reversed when the depolarizing agent was removed (Fig. 5A,B). Observing the same cells by TIRF microscopy, which has an axial resolution of ~100 nm, we could

detect overlap between ER-localized TMEM24–GFP and mitochondria in the submembrane space, indicating close proximity between the two structures (Fig. 5C). To test the hypothesis that TMEM24 may interact with mitochondria at ER–mitochondria contact sites, we utilized a membrane contact site reporter based on dimerization-dependent fluorescence (Alford et al., 2012). Briefly, the two monomers of a heteromeric fluorescent protein were anchored to the surface of the ER and mitochondria, respectively, and reconstitution of the red-light-emitting fluorescent protein only occurs when the two proteins are in proximity of each other, such as at contact sites between the ER and mitochondria (Fig. 5D; Fig. S3). When expressed in MIN6 cells, we observed red fluorescent structures that overlapped with MitoTracker, likely reflecting ER–mitochondria contacts (Fig. S3). Co-expression of TMEM24–GFP revealed little overlap under resting conditions, whereas accumulation at sites of ER–mitochondria proximity became apparent after depolarization-induced Ca²⁺ increases (Fig. 5E,F). These results show that TMEM24, in addition to acting at ER–PM contact sites, also might engage in reactions at ER–mitochondria contacts.

DISCUSSION

Previous work has established the ER-localized lipid-transport protein TMEM24 as an important regulator of insulin secretion from pancreatic β-cells (Lees et al., 2017; Pottekat et al., 2013). Transient reduction of TMEM24 expression or knockout of the TMEM24 gene have been found to impair insulin secretion from clonal rat and mouse β-cells. The underlying mechanism has been proposed to involve reduced Ca²⁺-independent recruitment of insulin granules to the PM (Pottekat et al., 2013) or disturbed regulation of voltage-dependent Ca²⁺ influx through alterations in the PM lipid composition (Lees et al., 2017). In this work, we further explored the mechanisms underlying TMEM24-dependent regulation of insulin secretion. In contrast to previous studies, we found that reduced expression of TMEM24 has little impact on voltage-dependent Ca²⁺ influx and only modestly impaired insulin secretion from β-cells. Instead, we identified TMEM24 as an important regulator of Ca²⁺ homeostasis at both the ER and the mitochondria, and show that this protein regulates mitochondrial ATP production.

TMEM24 is anchored to the ER through an N-terminal transmembrane domain and contains, in sequence, a lipid-binding SMP-domain, a C2-domain and a polybasic C-terminus. It is highly expressed in neuronal and endocrine tissue, including the pancreatic islets of Langerhans, where it is involved in tethering the ER to the PM (Lees et al., 2017; Sun et al., 2019). Its localization to the PM depends on electrostatic interactions between the C-terminus and negatively charged lipids in the PM, and neutralization of charged amino acids in TMEM24 by PKC-dependent phosphorylation results in TMEM24 dissociation. Using both intact and permeabilized cells, we found that the Ca²⁺-dependent dissociation of TMEM24 from the PM can be triggered even by nanomolar elevations of cytosolic Ca²⁺ through intracellular release or extracellular influx. Interestingly, we found that TMEM24 is already partially displaced from the PM under resting Ca²⁺ concentrations, perhaps due to constitutive PKC activity. This is consistent with findings from neuron-like cells, where endogenous TMEM24 has been found both at the PM and in the bulk ER under resting conditions (Sun et al., 2019). Such observations would support the hypothesis that TMEM24 acts at additional cellular locations, perhaps driven by interactions with lipids in the membranes of organelles known to form contacts with the ER (Cohen et al., 2018; Eden et al., 2010). By locally photobleaching a
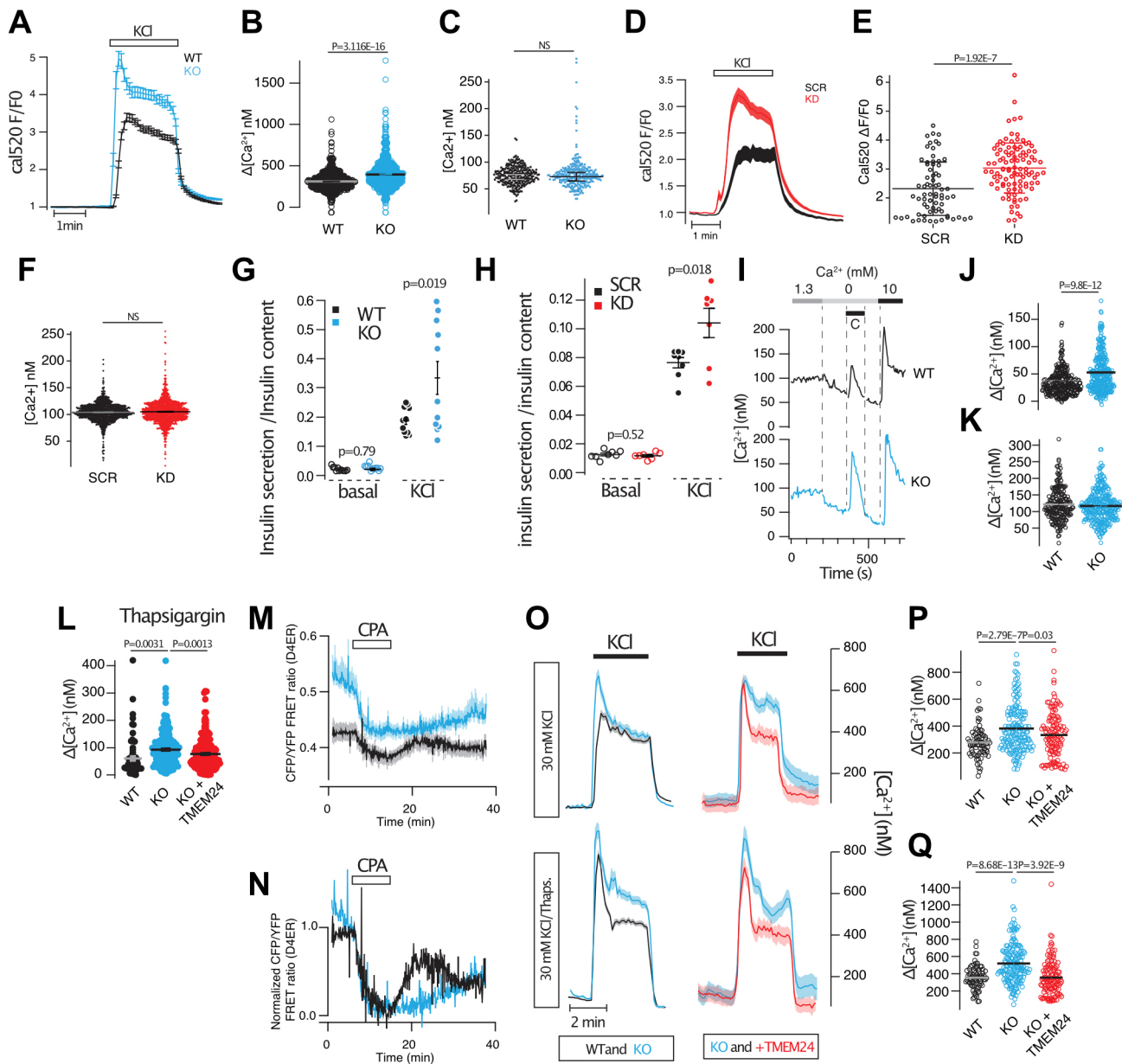
Fig. 3. See next page for legend.

small region of the PM in cells expressing TMEM24–GFP, we could also estimate the mobility of TMEM24 at ER–PM junctions. We found that TMEM24 weakly interacts with the PM, and that a large fraction was highly dynamic under resting conditions, which is in sharp contrast to E-Syt2, another SMP-domain-containing protein constitutively localized to ER-PM contact sites (Xie et al., 2019). This observation is also consistent with TMEM24 executing functions at other cellular locations than the PM.

In contrast to previous studies (Lees et al., 2017; Pottekat et al., 2013), we did not find support for an absolute requirement of TMEM24 for normal insulin secretion. Both transient knockdown of TMEM24 using siRNA and CRISPR/Cas9-mediated knockout of TMEM24 had little effect on either glucose- or depolarization-induced Ca²⁺ influx and insulin secretion from MIN6 cells cultured as monolayers. If anything, cells with reduced expression performed slightly better than control cells. Interestingly, when we instead allowed MIN6 cells to aggregate into islet-like cell clusters

(pseudo-islets) we found that the sustained glucose-stimulated insulin secretion was reduced following TMEM24 KO. One previous study, in which TMEM24 expression was stably reduced by shRNA, showed impaired glucose-stimulated insulin secretion from both clonal rat INS1 and mouse MIN6 β-cell pseudo-islets. The Ca²⁺ responses in these cells were normal, and secretion in response to direct depolarization was also unaffected by TMEM24 knockdown (Pottekat et al., 2013), which is similar to what we report here. CRISPR/Cas9-mediated knockout of TMEM24 in INS1 cells resulted in complete inhibition of both glucose-induced Ca²⁺ increases and insulin secretion, which was restored by re-expression of full-length TMEM24 (Lees et al., 2017). Although INS1 cells secrete insulin in response to glucose, the mechanism is likely different from that of primary β-cells in that it not only depends on K_{ATP}-channel closure (Herbst et al., 2002) and voltage-dependent Ca²⁺ influx (Dorff et al., 2002). Insulin secretion may instead be triggered by Ca²⁺ released from intracellular stores, since

Fig. 3. TMEM24 regulate ER Ca^{2+} homeostasis. (A) Depolarization-induced Ca^{2+}-influx in wild-type (black) and TMEM24 KO (blue) cells measured using Cal520. Traces are for 22 (WT) and 19 (KO) cells from one experiment for each condition. (B) Average cytosolic Ca^{2+} concentration change in response to 30 mM KCl in wild-type (black, n=298; N=9) and TMEM24 KO (blue, n=317; N=9) cells (unpaired two-tailed Student's t-test). (C) Resting Ca^{2+} concentration in wild-type (black, n=512; N=10) and TMEM24 KO (blue, n=534; N=10) cells determined using Fura-2 (unpaired two-tailed Student's t-test). (D) Depolarization-induced Ca^{2+} influx in control (SCR, black) and TMEM24 KD (KD, red) cells determined using Cal520. Traces are for 41 (SCR) and 54 (KD) cells from one experiment. (E) Average Cal520 fluorescence increase in response to 30 mM KCl in control (black, n=73; N=3) and TMEM24 KD (red, n=101; N=4) cells (unpaired two-tailed Student's t-test). (F) Resting Ca^{2+} concentration in control (black; n=419; N=8) and TMEM24 KD (red; n=396; N=8) cells determined by Fura-2 (NS, not significant; unpaired two-tailed Student's t-test). (G) Insulin secretion in wild-type (black) and TMEM24 KO (blue) cells exposed to buffers containing basal (5.5 mM) and depolarizing (30 mM) concentrations of KCl (n=12) (Kruskal–Wallis one-way analysis of variance and Mann–Whitney U-test). (H) Insulin secretion in control (black) and TMEM24 KD (red) cells exposed to buffers containing basal (5.5 mM) and depolarizing (30 mM) concentrations of KCl (n=8) (Kruskal–Wallis one-way analysis of variance and Mann–Whitney U-test). (I) Representative Fura-2 recordings showing cytosolic Ca^{2+} concentration changes in wild-type (black) and TMEM24 KO (blue) cells following ER-store depletion with 100 μM CPA and SOCE upon re-addition of 1.3 mM extracellular Ca^{2+}. (J) Quantifications of the increase in cytosolic Ca^{2+} in wild-type (black, n=296; N=6) and TMEM24 KO cells (blue, n=306; N=6) following addition of CPA shows that TMEM24 KO cells release more Ca^{2+} from the ER (unpaired two-tailed Student's t-test). (K) Quantifications of the increase in cytosolic Ca^{2+} in wild-type (black, n=296; N=6) and TMEM24 KO cells (blue, n=306; N=6) following SOCE shows that there is no difference between wild-type and TMEM24 KO cells (unpaired two-tailed Student's t-test). (L) Quantifications of the increase in cytosolic Ca^{2+} in response to 1 μM thapsigargin shows that more Ca^{2+} is released from the ER in TMEM24 KO cells (blue, n=270; N=6) compared to wild-type cells (black, n=77; N=3), and that this can be rescued by the re-expression of TMEM24 (red, n=248; N=6) (one-way ANOVA and Tukey's post hoc test). (M) Measurements of ER Ca^{2+} using D4ER following addition of 100 μM CPA shows that the resting ER Ca^{2+} concentration is higher in TMEM24 KO cells (blue) compared to wild-type cells (black) (for 5 cells for each condition from one experiment). (N) Resting D4ER FRET ratios in WT (black; n=18) and TMEM24 KO (blue; n=27) cells (unpaired two-tailed Student's t-test). (O) Average cytosolic Ca^{2+} concentration changes in wild-type (black), TMEM24 KO (blue) and TMEM24 KO cells with re-expression of TMEM24 (red) in response to 30 mM KCl alone (top row) or after 10 min treatment with 1 μM thapsigargin (bottom row). Data are from 32–43 cells from one experiment per condition. (P) Quantifications of the increase in cytosolic Ca^{2+} in wild-type (black, n=77; N=3) and TMEM24 KO cells (blue, n=277; N=6) following depolarization shows that there is a larger increase in TMEM24 KO cells that can be normalized by the re-expression of TMEM24 (red, n=270; N=6) (one-way ANOVA and Tukey's post hoc test). (Q) Quantifications of the increase in cytosolic Ca^{2+} in wild-type (black, n=77; N=3) and TMEM24 KO cells (blue, n=277; N=6) following depolarization in the presence of 1 μM thapsigargin shows that there is a larger increase in TMEM24 KO cells that can be normalized by the re-expression of TMEM24 (red, n=270; N=6) (one-way ANOVA and Tukey's post hoc test). WT, wild type. All data are presented as mean±s.e.m. (note in some cases error bars are too small to be visible).

addition of the ER Ca^{2+} ATPase (SERCA) inhibitor thapsigargin causes Ca^{2+} oscillations in these cells (Herbst et al., 2002). Another possibility for the observed differences in insulin secretion may be that TMEM24 only regulate secretion under certain conditions. The observation here that TMEM24 KO impaired sustained insulin secretion from pseudo-islets despite having little effect on glucose-induced cytosolic Ca^{2+} changes indicate that it may be involved in the amplifying pathways of insulin, which operate in parallel with the Ca^{2+}-dependent triggering pathway. The amplifying pathway requires mitochondrial metabolism, and is more prominent in pseudo-islets than cell monolayers (Chowdhury et al., 2013). Consistent with this, we observe impaired mitochondrial oxidative

phosphorylation in TMEM24 KO cells, which is accompanied by depolarization of the inner mitochondrial membrane and in hyper-accumulation of Ca^{2+}. The mitochondria were still able take up and release Ca^{2+} in response to changes in cytosolic Ca^{2+}, arguing against defects in the major uptake and extrusion pathways. Regulation of mitochondrial Ca^{2+} is closely linked to ER Ca^{2+}, and it is possible that the changes in mitochondrial function observed after TMEM24 KO are secondary to changes in ER Ca^{2+} handling. We found that TMEM24 KO cells have increased Ca^{2+} accumulation in the ER, observed by both measurements of cytosolic Ca^{2+} following ER-store depletion and by direct measurements of ER Ca^{2+}. It is not clear how TMEM24 contributes to ER Ca^{2+} homeostasis. The major route of Ca^{2+} uptake into the ER of β-cells is the SERCA (Roe et al., 1994) but we did not find any evidence for increased SERCA activity in TMEM24 KO cells. If anything, the activity was slightly reduced, as indicated by the lack of an initial Ca^{2+} lowering effect of glucose in TMEM24 KO cells, although this might also reflect impaired ATP production or the steeper concentration gradient in these cells. There is a continuous leakage of Ca^{2+} from the ER, which results in rapid loss of Ca^{2+} upon SERCA inhibition, but the mechanism behind this leak is not clear. Numerous mediators of ER Ca^{2+} leak have been identified, including presenilin-1/2 and TMCO1 (Tu et al., 2006; Wang et al., 2016). Reduced ER Ca^{2+} leak could explain the increased accumulation of Ca^{2+} in the ER of TMEM24 KO cells. Interestingly, loss of both presenilin-1 and TMCO1, like TMEM24, results in ER Ca^{2+} overload and in impaired mitochondria function (Tu et al., 2006; Wang et al., 2016, 2019). Although TMEM24 unlikely functions as a Ca^{2+} channel, it may modulate other release mechanisms either through direct interactions or modulation of the lipid environment. Because of its dynamic nature, TMEM24 may provide means to acutely regulate ER Ca^{2+} permeability in response to increases in cytosolic Ca^{2+} or PM DAG concentrations. An alternative explanation for how TMEM24 regulate mitochondria function is by acting in trans at ER-mitochondria contact sites. Increases in the cytosolic Ca^{2+} concentration causes the dissociation of TMEM24 from the PM and is followed by accumulation of TMEM24 at mitochondria, as shown by the increased overlap between TMEM24-GFP and an ER-mitochondria proximity reporter. This is similar to other ER-localized lipid transport proteins, such as ORP5/8 and Vps13A/C, which have been shown to bind more than one organelle membrane (Galmes et al., 2016; Kumar et al., 2018). Although our observations are consistent with a role of TMEM24 at ER-mitochondria contacts, this would need to be confirmed using super-resolution microscopy or correlative light and electron microscopy. ER-mitochondria contacts are sites of Ca^{2+} and lipid exchange that control mitochondria Ca^{2+} levels, ATP production and morphology in β-cells (Rieusset, 2018). It is possible that TMEM24 controls mitochondria Ca^{2+} by modulating the Ca^{2+} transfer reaction at ER-mitochondria contact sites. These contact sites concentrate many of the key components of organellar Ca^{2+} homeostasis, including the MCU, the voltage-dependent anion channel (VDAC), SERCA, Presenilin-1 and IP3 receptors (Area-Gomez et al., 2009; Vecellio Reane et al., 2020). The MCU has low affinity for Ca^{2+} and is kept inactive under resting cytosolic Ca^{2+} concentrations (Marchi and Pinton, 2014). However, MCU is still important for maintaining basal energy production, likely via sensing Ca^{2+} microdomains formed by Ca^{2+} release from the ER at ER-mitochondria contacts (Rossi et al., 2019). It is possible that TMEM24 controls the transfer of Ca^{2+} between the two compartments either by directly modulating the function of one or
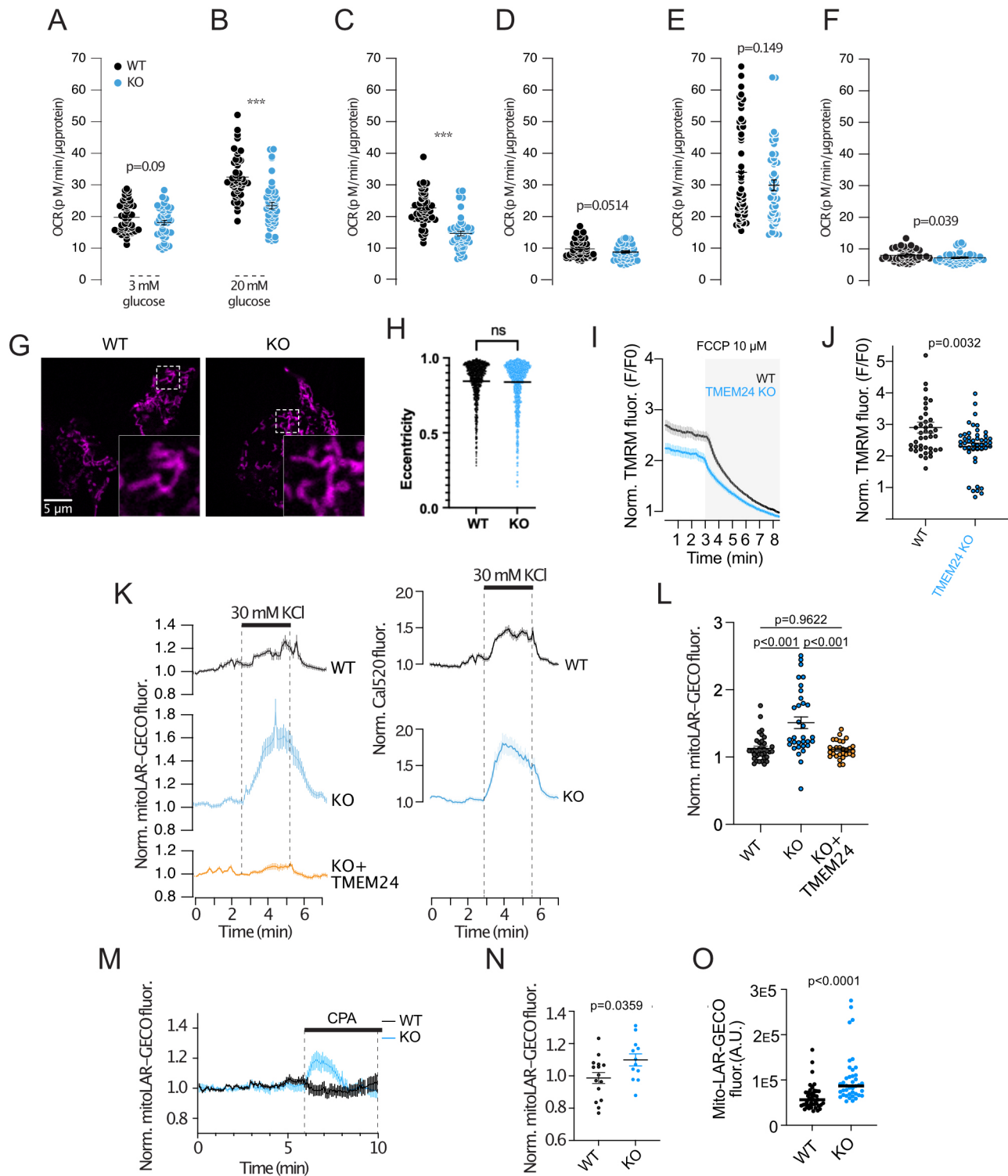
Fig. 4. See next page for legend.

several components of the contact sites, or indirectly through its effect on ER Ca^{2+} concentration and Ca^{2+} mobilization. Another intriguing possibility is that TMEM24 modulates the lipid composition of the mitochondria membranes, and that lack of this transport alters mitochondria function. TMEM24 has a strong preference for phosphatidylinositol, and the importance of this lipid for mitochondria function has been known since the 1960s (Vignais et al., 1963). More recently, it has been shown that that

the outer mitochondrial membrane is indeed rich in phosphatidylinositol (Zewe et al., 2020), and that phosphorylated derivatives of this lipid are required for mitochondrial function (Nagashima et al., 2020; Rosivatz and Woscholski, 2011). However, it remains to be discovered how phosphatidylinositol is delivered to the mitochondria. One possibility is that TMEM24 contributes to this transport and couples it to changes in Ca^{2+} concentration and energy demand. Interestingly, one study found

Fig. 4. TMEM24 controls mitochondria Ca²⁺ handling and ATP production. (A) Oxygen consumption rate (OCR) in wild-type (black) and TMEM24 KO (blue) cells at 3 mM glucose (n=40) (unpaired two-tailed Student's t-test). (B) OCR in wild-type (black) and TMEM24 KO (blue) cells at 20 mM glucose (n=40). OCR is reduced in TMEM24 KO cells (unpaired two-tailed Student's t-test). (C) ATP-coupled OCR in wild-type (black) and TMEM24 KO (blue) cells (n=40) (unpaired two-tailed Student's t-test). (D) Proton leak in wild-type (black) and TMEM24 KO (blue) cells (n=40) (unpaired two-tailed Student's t-test). (E) Maximal OCR in wild-type (black) and TMEM24 KO (blue) cells (n=40) (unpaired two-tailed Student's t-test). (F) Non-mitochondrial OCR in wild-type (black) and TMEM24 KO (blue) cells (n=40) (unpaired two-tailed Student's t-test). (G) Confocal microscopy images of wild-type (left) and TMEM24 KO (right) cells expressing the mitochondrial marker Tom20–mApple. Magnifications of the boxed areas are shown in the insets. (H) Measurements of the eccentricity of identified mitochondria in wild-type (black) and TMEM24 KO (blue) cells (n=918 mitochondria from 50 cells for WT and n=1037 mitochondria from 55 cells for KO, P=0.3965; unpaired two-tailed Student's t-test). (I) Epifluorescence microscopy recordings of TMRM fluorescence from wild-type (black) and TMEM24 KO (blue) cells in response to 10 µM FCCP which causes dissipation of the inner mitochondrial membrane potential. Data presented are for 40 (WT) and 46 (KO) cells from three experiments. (J) Resting TMRM fluorescence values in wild-type and TMEM24 KO cells after normalization to the fluorescence intensity in the presence of 10 µM FCCP (n=40–46 cells; P=0.0032; unpaired two-tailed Student's t-test). (K) Epifluorescence microscopy recordings of mito-LAR-GECO (left column) and Cal520 (right column) fluorescence from wild-type cells (black; n=36 cells), TMEM24 KO cells (blue; n=32 cells) and TMEM24 KO cells with re-expression of TMEM24 (yellow; n=32 cells). (L) Mito-LAR-GECO fluorescence change in response to 30 mM KCl in wild-type cells (black; n=40; N=8), TMEM24 KO cells (blue; n=42; N=7) and TMEM24 KO cells with re-expression of TMEM24 (yellow; n=29; N=7). P<0.0001 for KO versus WT and P=0.9622 for WT versus rescue (one-way ANOVA and Tukey's post hoc test). (M) Epifluorescence microscopy recordings of mito-LAR-GECO fluorescence from wild-type (black; n=15) and TMEM24 KO (blue; n=12) cells. (N) Mito-LAR-GECO fluorescence change in response to 100 µM CPA in wild-type (black, n=15; N=3) and TMEM24 KO (blue; n=12; N=3) cells (P=0.0359, unpaired two-tailed Student's t-test). (O) Resting mito-LAR-GECO fluorescence intensity in wild-type (black; n=50; N=8) and TMEM24 KO (blue; n=43; N=8) cells (P<0.0001, unpaired two-tailed Student's t-test). WT, wild type. All data are presented as mean±s.e.m. (note in some cases error bars are too small to be visible). ***P<0.001; ns, not significant.

that depletion or masking of PI(4,5)P₂ on the mitochondria surface caused mitochondrial fragmentation, which could be prevented by PKC activation and would also trigger TMEM24 dissociation from the PM to enable interactions with the mitochondria (Rosivatz and Woscholski, 2011). A Ca²⁺-dependent feedback system to control mitochondria function may be particularly important in the β-cells, where mitochondrial metabolism is tightly coupled to Ca²⁺ influx in order to adjust insulin secretion and maintain blood glucose homeostasis.

MATERIALS AND METHODS
Plasmids and reagents
Plasmids for expression of TMEM24–EGFP (Lees et al., 2017), E-Syt1–GFP (Giordano et al., 2013) and mRFP–PH-PLCδ1 were gifts from Pietro De Camilli (Yale University, New Haven, Connecticut, USA), as were those for ER–oxGFP, GFP–CAAX and E-Syt2–GFP (Giordano et al., 2013). VAMP2–pHluorin and NPY–mCherry were gifts from Sebastian Barg (Uppsala University, Uppsala, Sweden). GFP–P4M-SidM was Addgene plasmid #51472 (deposited by Gerald Hammond, University of Pittsburgh; Hammond et al., 2014). GFP–C1aC1b_PKC_ was a gift from Anders Tengholm (Uppsala University; Wuttke et al., 2013). R-GECO and mito-LAR-GECO were Addgene plasmids #32444 and #61245 (deposited by Robert Campbell, University of Alberta, Edmonton, Canada; Wu et al., 2014; Zhao et al., 2011). mApple–Tomm20 was Addgene plasmid #54955 (deposited by Michel Davidson). TMEM24–mCherry was generated by PCR amplification of human TMEM24 with flanking Nhe1 and EcoR1

followed by ligation into the mCherry-N1 vector (gift from Pietro De Camilli) using the following primers: TMEM24-Nhe1-fwd, 5′-CTAGCTAGCCATGGATCCGGGCTGGGGGCA-3′; TMEM24-EcoR1-rev, 5′-CCGGAATTCTGAGCTGGGGGCTGGGGTT-3′. RA-Sec61b and GB-Dcp1b Addgene plasmids #153978 and #153979 (deposited by Gia Voeltz; Lee et al., 2020). GB was PCR-amplified using a 5′ primer containing a AgeI site, 5′-CGCTAGCACCGGTGGCCACCATCA-3′ as well as a 3′ primer containing a NotI site and a stop codon, 5′-GCGGCCGCTTATCCGGACTTGTACC-3′. The PCR-generated fragment was subcloned into the AgeI/NotI sites of the TOM20–mApple vector, replacing the mApple sequence and forming a tandem TOM20-GB construct. All salts, HEPES, poly-L-lysin, EGTA, α-toxin, thapsigargin, nitrilotriacetic acid (NTA) and diazoxide were from Sigma-Aldrich. DMEM, penicillin, streptomycin, glutamine and fetal bovine serum (FBS) were from Life Technologies. Carbachol, phorbol 12-myristate 13-acetate (PMA), cyanide-p-trifluoromethoxyphenylhydrazone (FCCP), rotenone, antimycin A and cyclopiazonic acid (CPA) were from Sigma-Aldrich. Bafilomycin was from TOCRIS Bioscience. Fluo-4-AM, Fura-2-AM and TMRM were from Life Technologies. Cal-520-AM and Cal590-AM were from AAT Bioquest.

Cell culture and transfection for imaging
The mouse β-cell line MIN6 (passages 18–30; gift from Jun-ichi Miyazaki, Kumomoto University, Japan) (Miyazaki et al., 1990) was cultured in DMEM (Life Technologies) supplemented with 25 mmol/l glucose, 15% FBS, 2 mmol/l L-glutamine, 50 µmol/l 2-mercaptoethanol, 100 U/ml penicillin and 100 µg/ml streptomycin (complete culture medium). The cells were kept at 37°C and 5% CO₂ in a humidified incubator. Prior to imaging, $0.2×10^6$ cells were resuspended in 100 µl Opti-MEM-I medium (Life Technologies) with 0.2 µg plasmid (total) and 0.5 µl Lipofectamine 2000 (Life Technologies) and seeded in the center of a 25-mm poly-L-lysine-coated coverslip. The transfection reaction was terminated after 4–6 h by the addition of 2 ml complete culture medium and cells were imaged 18–24 h later. MIN6 pseudo-islets were generated by resuspending $1×10^6$ MIN6 cells in 1 ml complete culture medium and seeding them into a non-stick 12-well cell culture plate (Falcon plastics, VWR, Sweden) followed by culturing for 48–72 h at 37°C and 5% CO₂ in a humidified incubator. This resulted in the spontaneous formation of islet-like cell clusters. Cell cultures were routinely tested for mycoplasma infections (Eurofins genomics).

α-Toxin permeabilization
Transfected MIN6 cells, grown on 25-mm poly-L-lysine-coated glass coverslips, were incubated with 0.5 µM of the AM-ester form of Cal520 (AAT Bioquest, Sunnyvale, CA) for 30 min at 37°C. The coverslips were subsequently used as exchangeable bottoms in a modified Sykes–Moore open superfusion chamber that was mounted on the stage of a TIRF microscope (described below) and connected to a peristaltic pump that allowed rapid change of medium. Following a change from normal, extracellular-like, medium (125 mM NaCl, 4.9 mM KCl, 1.3 mM MgCl₂, 1.2 mM CaCl₂, 25 mM HEPES, 1 mg/ml BSA with pH set to 7.4) to an intracellular-like medium (see below), the superfusion was interrupted and α-toxin was added directly to the chamber (final concentration ≈50 µg/ml). Permeabilization was considered complete when the Cal520 fluorescence had decreased by >90%, which typically took 2–5 min. Superfusion was then started again and the cells were exposed to intracellular-like buffers containing calibrated Ca²⁺ concentrations while fluorescence from both remaining Cal520 and mCherry-tagged fusion proteins was recorded. These experiments were performed at ambient temperature (21–23°C).

Intracellular-like medium
Intracellular-like medium with buffered pH, [Ca²⁺] and [Mg²⁺] used in α-toxin permeabilization experiments contained: 6 mM Na⁺, 140 mM K⁺, 1 mM (free) Mg²⁺, 0–100 µM (free) Ca²⁺, 1 mM Mg-ATP, 10 mM HEPES, 2 mM (total) EGTA and 2 mM (total) nitrilotriacetic acid (NTA) with pH adjusted to 7.00 at 22°C with 2 M KOH. The total concentration of Ca²⁺ and Mg²⁺ was calculated using the online version of MaxChelator (http://www.stanford.edu/~cpatton/webmaxcS.htm). Media were made fresh
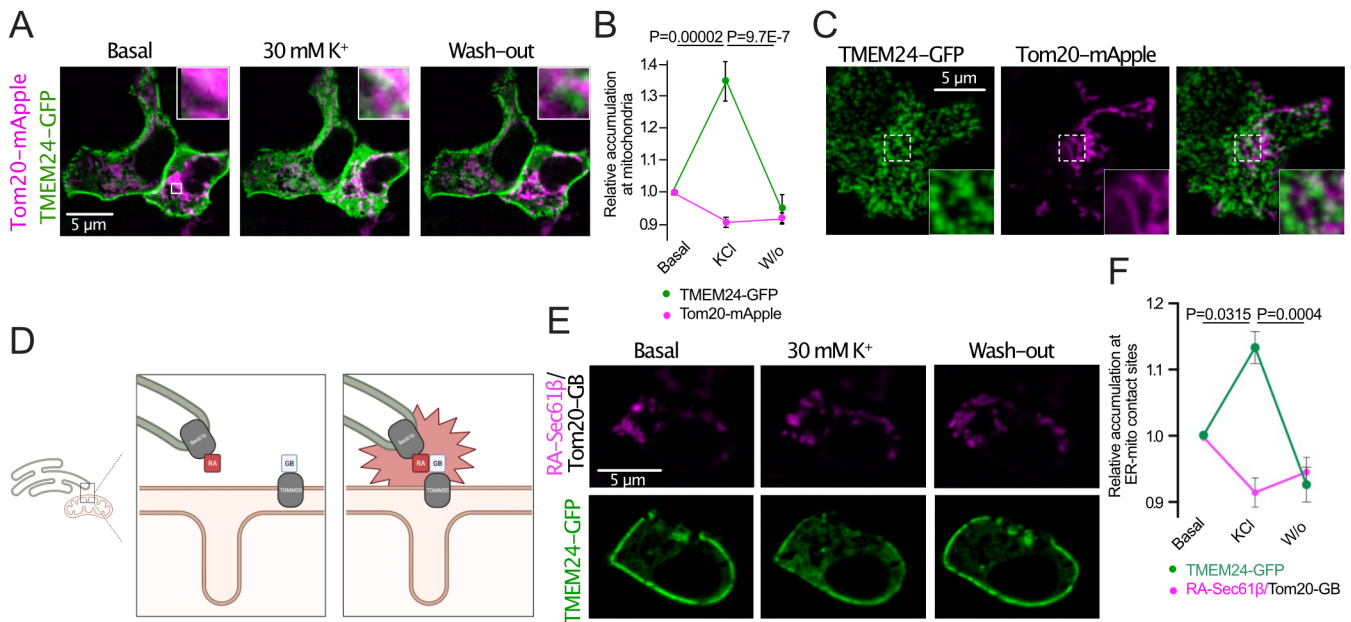
Fig. 5. Enrichment of TMEM24 at sites of ER-mitochondria proximity. (A) Confocal microscopy images of a MIN6 cell expressing mApple–Tom20 (magenta) and TMEM24–GFP (green) under resting conditions, during stimulation with 30 mM KCl and following washout (W/o) of the depolarizing stimuli. Boxed area is magnified in the upper right corner. (B) Quantification of TMEM24–GFP fluorescence overlap with mApple–Tom20-positive mitochondria before, during and after depolarization with 30 mM KCl (green). Changes in corresponding mApple–Tom20 fluorescence is shown as a control for bleaching (magenta). Data presented as mean±s.e.m. (n=24; N=8; paired two-tailed Student's t-test). (C) TIRF micrographs of a MIN6 cell expressing TMEM24–GFP (green) and mApple–Tom20 (magenta). (D) Principle of detection of ER-mitochondria contact sites using ER-targeted RA (Sec61β-RA) and mitochondria-anchored GB (GB-Tom20). (E) Confocal microscopy images of a MIN6 cell expressing Sec61β-RA and GB-Tom20 (magenta) and TMEM24–GFP (green) under resting conditions, during depolarization with 30 mM KCl and following washout of the depolarizing stimuli. (F) Quantification of TMEM24–GFP fluorescence overlap with the ER–mitochondria contact site reporter before, during and after depolarization with 30 mM KCl (green). Changes in corresponding contact site marker fluorescence is shown as a control for bleaching (magenta). Data presented as mean±s.e.m. (n=12; N=4; Kruskal–Wallis one-way analysis of variance and Mann–Whitney U-test).

on the day of experiment and kept on ice. To validate the media composition, cells loaded with the Ca^{2+} indicator Cal520 were mounted on a TIRF microscope, permeabilized and exposed to media with increasing Ca^{2+} concentrations. From these data a dose–response curve was generated and the EC_{50} for Ca^{2+}-binding to Cal520 was estimated to be 980 nM, an *in situ* estimation 3-fold higher than the reported *in vitro* K_D of 320 nM.

TMEM24 knockdown by siRNA

MIN6 cells were resuspended with 25 nM antiTMEM24 siRNA smartpool (Dharmacon, siGENOME cat. no. L-061885-01-0020) pre-mixed with 1.6 µl/ml Lipofectamine RNAiMAX (Life Technologies) in Opti-MEM I medium. After 3 h, the Opti-MEM I medium was replaced by DMEM growth medium containing 25 nM siRNA and 1.6 µl/ml Lipofectamine 3000 (Life Technologies) and incubated overnight. Cells transfected with a scrambled sequence siRNA (Dharmacon, siGENOME) following the same procedure were used as controls. After 48 h, cells were transfected for imaging as described above. The knockdown efficiency was evaluated by western blotting and real-time PCR (see below).

Generation of TMEM24 KO MIN6 cells by CRISPR/Cas9

TMEM24 KO MIN6 were generated using a mix of three TMEM24 CRISPR/Cas9 plasmids (Santa Cruz Biotechnology, sc-428047), containing GFP and the following gRNAs: 5′-TTACCATGGTGCGCTCT-GAT-3′, 5′-CAGCACTCAGCCCGCCATGA-3′ and 5′-GTCCCCCGCT-GCCGTCTCCA-3′. TMEM24 CRISPR/Cas9 plasmids were transfected into MIN6 by Lipofectamine 3000 (Thermo Fisher, L3000015). After 24-h, single cells positive (knockout) and negative (control) for GFP were sorted using a BD FACSariaIII CellSorter and subsequently plated into 96-well plates. Cells were cultured in standard MIN6 growth medium. The clones were tested for the presence of TMEM24 by western blotting utilizing anti-TMEM24 antibody (Thermo Fisher, A304-764A; 1:1000).

TIRF and confocal microscopy

A medium containing 125 mM NaCl, 4.9 mM KCl, 1.3 mM $MgCl_2$, 1.2 mM $CaCl_2$, 25 mM HEPES, 1 mg/ml BSA with pH set to 7.4 at 37°C was used in all microscopy experiments. Cells were pre-incubated in this medium supplemented with 3 mM glucose for 30 min followed by perifusion with the same medium during recordings. A previously described custom-build prism-type TIRF microscope setup equipped with a 16×/0.8 NA water immersion objective (Nikon) was used to observe large populations of cells (Idevall-Hagren et al., 2010). It was built around an E600FN upright microscope (Nikon) enclosed in a Perspex box thermostated at 37°C. 491-nm and 561-nm DPSS lasers (Cobolt, Sweden) were used to excite GFP and mCherry, respectively. The laser beams were merged by dichroic mirrors (Chroma Technology) and homogenized by a rotating light shaping diffuser (Physic Optics Corps) before being refocused through a dove prism (Axicon) with a 70° angle to achieve total internal reflection. Laser lines were selected with interference filters (Semrock) in a motorized filter wheel equipped with a shutter (Sutter Instruments) blocking the beam between image captures. Emission light was detected at 530/50 nm (Semrock interference filters) for GFP or 597LP (Melles Griot glass filter) for mCherry using a CCD camera (Hamamatsu ORCA-AG) controlled by MetaFluor software (Molecular Devices). For high-resolution TIRF imaging, we used an Eclipse TiE microscope (Nikon) equipped with a TIRF illuminator and a 60×/1.45 NA or 100×/1.49 NA objectives as previously described (Xie et al., 2019). Confocal microscopy was performed on an Eclipse TE2000 microscope (Nikon) equipped with a Yokogawa CSU-10 spinning disc confocal unit and a 100×/1.49 NA plan Apochromat objective (Nikon) (Idevall-Hagren et al., 2013). Briefly, GFP and mCherry were excited by 491-nm and 561-nm DPSS lasers (Cobolt, Sweden) and were detected through 530/50 nm interference filter and 597LP filter, respectively, through a black-illuminated EM-CCD camera (DU-888; Andor Technology).

Fluorescence recovery after photobleaching

TIRF-FRAP was performed on a Nikon TiE microscope equipped with an iLAS2 TIRF illuminator for multi-angle patterned illumination (Cairn Research) and a 100×/1.49 NA Apo-TIRF objective. Excitation light for GFP and mCherry was delivered by 488-nm and 561-nm diode-pumped solid-state lasers with built-in acousto-optical modulators, and light for bleaching was delivered by a 405-nm DPSS laser (all from Coherent). Fluorescence was detected with a back-illuminated EMCCD camera (DU-897, Andor Technology) controlled by MetaMorph (Molecular Devices). Emission wavelengths were selected with filters (527/27 nm for GFP and 590 nm long-pass for mCherry) mounted in a filter wheel (Sutter Instruments). Cells were mounted in an open perfusion chamber with temperature held at 37°C. Following a 10 s baseline acquisition, a 3×3 μm area within the cells was exposed to a 100 ms 405-nm light pulse to bleach the fluorophores, followed by continued acquisition for 120 s at 4 fps. Calculations of the mobile fraction (Mf) of each fluorescent protein was performed using the following formula:

$$Mf = 100 \times \frac{(Fpc - Fbg)}{(F\infty c - Fbg)} \times \frac{((F\infty - Fbg) - (F0 - Fbg))}{((Fp - Fbg) - (F0 - Fbg))}, \quad (1)$$

where Fpc is whole cell pre-bleach intensity, Fp is bleach region of interest (ROI) pre-bleach intensity, $F\infty c$ is asymptote of fluorescence recovery of the whole cell, Fbg is mean background intensity, $F\infty$ is asymptote of the bleach ROI, and $F0$ is bleach ROI post-bleach intensity.

Western blot analysis

After three washes with phosphate-buffered saline (PBS), MIN6 cells were homogenized and lysed in RIPA buffer (50 mM Tris-HCl, pH=7.4, 1% NP-40, 0.5% sodium deoxycholate, 0.1% SDS and 150 mM EDTA), placed on ice for 30 min or agitated on a rotator at 4°C for 30 min. Cell lysates were mixed with 3× sample buffer (6% SDS, 15% 2-mercaptoethanol, 30% glycerol, 0.006% Bromophenol Blue and 0.15 M Tris-HCl) and boiled at 95°C for 10 min. Protein content was determined by a detergent-compatible protein assay (Bio-Rad, Hercules, CA, USA) and proteins were separated by SDS-PAGE (5–20%) and blotted onto PVDF membrane using semi-dry transfer. Membranes were blocked in 4% milk dissolved in Tris-buffered saline with 0.1% Tween 20. The following antibodies and dilutions were used: anti-TMEM24 (Bethyl Laboratories, A304-764, 1:1000, specificity confirmed by KD and KO in this study), anti-GAPDH (Cell Signaling Technology, 14C10, 1:1000), anti-rabbit-IgG secondary antibody (GE Healthcare, 1:10,000). Membranes were developed with the Odyssey Fc Imaging system (LI-COR Bioscience).

Quantitative RT-PCR

mRNA from control and TMEM24 knockdown cells were extracted using the NucleoSpin RNAPlus kit (Macherey-Nagel). RT-PCR was performed by QuantiTect SYBR Green RT-PCR kit (Qiagen) using the following primer: GAPDH-fwd, 5′-ACTCCACTCACGGCAAATTC-3′; GAPDH-rev, 5′-TCTCCATGGTGGTGAAGACA-3′; TMEM24-fwd, 5′-CGCCCA-GAACTCAGCCTAAA, TEME24-rev, 5′-GGGTAGGTCTGGGGATG-GAT-3′. The PCR was performed in a Light Cycler 2.0 (Roche). Results are presented as $\Delta\Delta C_t$, normalized to GAPDH expression in control and TMEM24 KD cells.

Insulin secretion measurements

Insulin secretion was measured from monolayers of MIN6 cells grown in 12-well plates. 4×10^5 control or TMEM24 knockdown cells were prepared as described above in 12-well plates 72 h before secretion measurements. Cells were pre-incubated in 3 mM glucose imaging buffer at 37°C for 30 min. Cells were subsequently incubated in buffers containing 3 mM glucose, 20 mM glucose or 3 mM glucose supplemented with 30 mM KCl, immediately followed by buffer collection. In the end, cells were released by the addition of 80 μl typsin and mixed with 120 μl complete growth medium. 100 μl of the collected cell suspension was mixed with 100 μl acidic ethanol, sonicated on ice and neutralized by the addition of 900 μl Tris buffer (pH 8) to determine insulin content. The insulin concentration in the samples was measured by a mouse insulin AlphaLISA kit (Perkin-Elmer). For perifusion experiments,

groups of 30 pseudo-islets were placed in a 10 μl teflon tube chamber and perifused at a rate of 60 μl/min using a pressurized air system (AutoMate Scientific, Berkeley, CA, USA) and equilibrated in experimental buffer containing 3 mM glucose during 45 min. The perifusate was subsequently collected in 5-min fractions into ice-chilled 96-well plates with a non-binding-surface (Corning Inc Kennebuk, ME) while changing the glucose concentration to 20 mM. The islets were retrieved and briefly sonicated in acid ethanol to determine insulin content. Insulin concentrations in the samples were determined with ELISA according to the manufacturer's instructions (Mercodia AB, Uppsala, Sweden).

Oxygen consumption rates measurement

The oxygen consumption rate (OCR) in MIN6 cells were monitored by an Extracellular Flux Analyzer (XFe96, Agilent Technologies, CA, USA). 3×10^4 cells (wild-type and TMEM24 KO) were seeded in each well of XFe96 microplates and cultured for an additional 24 h. Cells were thereafter pre-incubated with Seahorse XF DMEM (Agilent Technologies) containing 3 mM glucose (pH 7.4) for 1 h at 37°C before the microplate was inserted into the XFe96 Analyzer. For each experiment, 4–6 replicates of each treatment were measured. OCR at 3 mM glucose was measured for 30 min, followed by another 30 min with either 3 mM or 20 mM glucose. Then, the proportions of respiration driving ATP synthesis and proton leak were determined by blocking ATP synthase with 2 μM oligomycin (Sigma-Aldrich). Subsequently, 2 μM of the mitochondrial uncoupler cyanide-p-trifluoromethoxyphenylhydrazone (FCCP) was added to determine the maximal respiratory capacity. Finally, 2 μM rotenone and 5 μM antimycin A were added together to block transfer of electrons from the mitochondrial respiratory chain complex I and III to determine the remaining non-mitochondria-dependent respiration. To calculate the mitochondrial respiration, non-mitochondrial OCR was subtracted from the total OCR. Data was normalized to protein content which was determined by the DC protein assay (Bio-Rad Laboratories, USA).

Measurements of mitochondrial membrane potential

The mitochondrial membrane potential ($\Delta\Psi_m$) was monitored by the lipophilic cationic dye tetramethylrhodamine methyl ester (TMRM) via fluorescence time-lapse imaging using an inverted microscope (Eclipse TE2000U; Nikon, Kanagawa, Japan). The epifluorescence microscope is equipped with a high-power LED light source (Omicron LedHUB; Photonlines Ltd, Newcastle, UK) which, connected with a 5-mm diameter liquid light guide, provided excitation light at 540 nm. Emission was measured at 560 nm (5 nm half-bandwidth) and the fluorescence signal was detected by an Evolve EMCCD camera (Photometrics, Arizona, USA). MetaFluor software (Molecular Devices Corp.), which was allowed to control the microscope setup and to acquire images every 5 s. Prior to imaging, the cells were seeded onto 25 mm round coverslips and loaded with TMRM at 10 nM during a 30-min incubation at 37°C in an imaging buffer containing 125 mM NaCl, 5 mM KCl, 1.3 mM CaCl$_2$, 1.2 mM MgCl$_2$, and 25 mM HEPES with pH adjusted to 7.40 with NaOH. The coverslips were placed on the bottom of an open Sykes–More chamber. On the top of the coverslip, a thin 25-mm diameter stainless steel plate with a 4-mm wide and 7-mm long opening pressed the 1-mm thick silicon rubber gasket with identical dimensions and central opening to the coverslip. The temperature of the chamber holder and the CFI S Fluor 40×/1.3 NA oil immersion objective (Nikon) was stable at 37°C during the experiment using custom-built thermostats. Fixed on the stainless-steel plate, inlet and outlet cannulas maintained a laminar superfusion at a rate of 2.0 ml/min with the imaging buffer containing 10 nM TMRM.

Measurement of cytoplasmic, mitochondrial and ER [Ca^{2+}]

Cytosolic [Ca^{2+}] was measured on an epifluorescence microscope setup (described above) using the ratiometric dye Fura-2 or the green-fluorescent dye Cal520. The cells were preincubated for 30 min at 37°C in imaging buffer supplemented with 1 μM of the AM-ester-form of the indicator, followed by repeated washing in imaging buffer and imaging. Mitochondrial Ca^{2+} was measured using the genetically encoded red fluorescence, low-affinity indicator mito-LAR-GECO (Wu et al., 2014), whereas ER Ca^{2+} was

measured using the FRET-based indicator D4ER (Ravier et al., 2011). Both indicators were delivered to cells by transient transfection as described above, and experiments were performed 18–36 h post transfection.

Morphometric analysis of mitochondria

To determine the morphology of the mitochondria, wild-type MIN6 cells and TMEM24 KO cells expressing mApple–Tom20 were observed under the spinning disc confocal microscope. The images were analyzed with the open-source image analysis software CellProfiler (Carpenter et al., 2006) using several modules that were placed in a sequential order to create a flexible image analysis pipeline. First, processing filters were applied to enhance the fluorescence signal of the regions that display higher intensity relative to its immediate neighborhood. This allowed the better identification of the mitochondria as separate objects during the following module. The Otsu's automatic threshold method permitted the assignment of the threshold value by including the pixels of the image either in the 'background' class or the 'foreground' class. The objects/mitochondria detected using the pipeline were not de-clumped to enable the identification of potential network formation, and the size and shape of the mitochondria was determined and the data was exported to Microsoft Excel. Eccentricity, which distinguish mitochondria based on shape from tubular (1) to circular (0), was used as an overall determinant of the mitochondria shape.

Image analysis

TIRF microscopy and confocal microscopy images were analyzed offline by Fiji (Schindelin et al., 2012). To determine fluorescence changes, the ROIs and background regions were first manually identified. Fluorescence intensity changes within these regions were recorded and the data was exported to Excel. All data points were background corrected and normalized to the initial fluorescence intensity (F/F_0).

Statistical analysis

One-way ANOVA followed by Tukey's post hoc test (for normally distributed data), Kruskal–Wallis one-way ANOVA followed by a Mann–Whitney U-test (for non-parametric data) or a two-tailed (paired or unpaired) Student's t-test were used. All data presented are from at least three biological replicates. For imaging data, n numbers represent individual cells and N numbers represents independent experiments. For all other data presented, n numbers indicate independent observations.

References

Alford, S. C., Abdelfattah, A. S., Ding, Y. and Campbell, R. E. (2012). A fluorogenic red fluorescent protein heterodimer. Chem. Biol. 19, 353-360. doi:10.1016/j.chembiol.2012.01.006

Area-Gomez, E., De Groof, A. J. C., Boldogh, I., Bird, T. D., Gibson, G. E., Koehler, C. M., Yu, W. H., Duff, K. E., Yaffe, M. P., Pon, L. A. et al. (2009). Presenilins are enriched in endoplasmic reticulum membranes associated with mitochondria. Am. J. Pathol. 175, 1810-1816. doi:10.2353/ajpath.2009.090219

Balla, T. (2018). Ca^{2+} and lipid signals hold hands at endoplasmic reticulum–plasma membrane contact sites. J. Physiol. 596, 2709-2716. doi:10.1113/JP274957

Bian, X., Saheki, Y. and De Camilli, P. (2018). Ca^{2+} releases E-Syt1 autoinhibition to couple ER -plasma membrane tethering with lipid transport. EMBO J. 37, 219-234. doi:10.15252/embj.201797359

Carpenter, A. E., Jones, T. R., Lamprecht, M. R., Clarke, C., Kang, I. H., Friman, O., Guertin, D. A., Chang, J. H., Lindquist, R. A., Moffat, J. et al. (2006). CellProfiler: image analysis software for identifying and quantifying cell phenotypes. Genome Biol. 7, R100. doi:10.1186/gb-2006-7-10-r100

Chen, L., Koh, D.-S. and Hille, B. (2003). Dynamics of calcium clearance in mouse pancreatic β-cells. Diabetes 52, 1723-1731. doi:10.2337/diabetes.52.7.1723

Chowdhury, A., Dyachok, O., Tengholm, A., Sandler, S. and Bergsten, P. (2013). Functional differences between aggregated and dispersed insulin-producing cells. Diabetologia 56, 1557-1568. doi:10.1007/s00125-013-2903-3

Chung, W. Y., Jha, A., Ahuja, M. and Muallem, S. (2017). Ca2+ influx at the ER/PM junctions. Cell Calcium 63, 29-32. doi:10.1016/j.ceca.2017.02.009

Cohen, S., Valm, A. M. and Lippincott-Schwartz, J. (2018). Interacting organelles. Curr. Opin. Cell Biol. 53, 84-91. doi:10.1016/j.ceb.2018.06.003

Dorff, G., Grapengiesser, E. and Hellman, B. (2002). Insulin-secreting INS-1 cells generate a novel type of poorly synchronized Ca2+ transients. Biochem. Biophys. Res. Commun. 293, 842-846. doi:10.1016/S0006-291X(02)00311-X

Eden, E. R., White, I. J., Tsapara, A. and Futter, C. E. (2010). Membrane contacts between endosomes and ER provide sites for PTP1B-epidermal growth factor receptor interaction. Nat. Cell Biol. 12, 267-272. doi:10.1038/ncb2026

Galmes, R., Houcine, A., Vliet, A. R., Agostinis, P., Jackson, C. L. and Giordano, F. (2016). ORP5/ORP8 localize to endoplasmic reticulum–mitochondria contacts and are involved in mitochondrial function. EMBO Rep. 17, 800-810. doi:10.15252/embr.201541108

Giordano, F., Saheki, Y., Idevall-Hagren, O., Colombo, S. F., Pirruccello, M., Milosevic, I., Gracheva, E. O., Bagriantsev, S. N., Borgese, N. and De Camilli, P. (2013). PI(4,5)P2-dependent and Ca^{2+}-regulated ER-PM interactions mediated by the extended synaptotagmins. Cell 153, 1494-1509. doi:10.1016/j.cell.2013.05.026

Hammond, G. R. V., Machner, M. P. and Balla, T. (2014). A novel probe for phosphatidylinositol 4-phosphate reveals multiple pools beyond the Golgi. J. Cell Biol. 205, 113-126. doi:10.1083/jcb.201312072

Herbst, M., Sasse, P., Greger, R., Yu, H., Hescheler, J. and Ullrich, S. (2002). Membrane potential dependent modulations of calcium oscillations in insulin-secreting INS-1 cells. Cell Calcium 31, 115-126. doi:10.1054/ceca.2001.0266

Idevall-Hagren, O., Barg, S., Gylfe, E. and Tengholm, A. (2010). cAMP mediators of pulsatile insulin secretion from glucose-stimulated single β-cells. J. Biol. Chem. 285, 23007-23018. doi:10.1074/jbc.M109.095992

Idevall-Hagren, O., Jakobsson, I., Xu, Y. and Tengholm, A. (2013). Spatial control of Epac2 activity by cAMP and Ca2+-mediated activation of ras in pancreatic β cells. Sci. Signal. 6, ra29. doi:10.1126/scisignal.2003932

Idevall-Hagren, O., Lü, A., Xie, B. and De Camilli, P. (2015). Triggered Ca^{2+} influx is required for extended synaptotagmin 1-induced ER-plasma membrane tethering. EMBO J. 34, 2291-2305. doi:10.15252/embj.201591565

Johnson, B., Leek, A. N., Solé, L., Maverick, E. E., Levine, T. P. and Tamkun, M. M. (2018). Kv2 potassium channels form endoplasmic reticulum/plasma membrane junctions via interaction with VAPA and VAPB. Proc. Natl. Acad. Sci. USA 115, E7331-E7340. doi:10.1073/pnas.1805757115

Kumar, N., Leonzino, M., Hancock-Cerutti, W., Horenkamp, F. A., Li, P. Q., Lees, J. A., Wheeler, H., Reinisch, K. M. and De Camilli, P. (2018). VPS13A and VPS13C are lipid transport proteins differentially localized at ER contact sites. J. Cell Biol. 217, 3625-3639. doi:10.1083/JCB.201807019

Lee, J. E., Cathey, P. I., Wu, H., Parker, R. and Voeltz, G. K. (2020). Endoplasmic reticulum contact sites regulate the dynamics of membraneless organelles. Science 367, eaay7108. doi:10.1126/science.aay7108

Lees, J. A., Messa, M., Sun, E. W., Wheeler, H., Torta, F., Wenk, M. R., De Camilli, P. and Reinisch, K. M. (2017). Lipid transport by TMEM24 at ER-plasma membrane contacts regulates pulsatile insulin secretion. Science 355, eaah6171. doi:10.1126/science.aah6171

Marchi, S. and Pinton, P. (2014). The mitochondrial calcium uniporter complex: molecular components, structure and physiopathological implications. J. Physiol. 592, 829-839. doi:10.1113/jphysiol.2013.268235

Miyazaki, J. I., Araki, K., Yamato, E., Ikegami, H., Asano, T., Shibasaki, Y., Oka, Y. and Yamamura, K.-I. (1990). Establishment of a pancreatic β cell line that retains glucose-inducible insulin secretion: special reference to expression of glucose transporter isoforms. Endocrinology 127, 126-132. doi:10.1210/endo-127-1-126

Nagashima, S., Tábara, L.-C., Tilokani, L., Paupe, V., Anand, H., Pogson, J. H., Zunino, R., McBride, H. M. and Prudent, J. (2020). Golgi-derived PI(4)P-containing vesicles drive late steps of mitochondrial division. Science 367, 1366-1371. doi:10.1126/science.aax6089

Pottekat, A., Becker, S., Spencer, K. R., Yates, J. R., Manning, G., Itkin-Ansari, P. and Balch, W. E. (2013). Insulin biosynthetic interaction network component, TMEM24, facilitates insulin reserve pool release. *Cell Rep.* **4**, 921-930. doi:10.1016/j.celrep.2013.07.050

Ravier, M. A., Daro, D., Roma, L. P., Jonas, J.-C., Cheng-Xue, R., Schuit, F. C. and Gilon, P. (2011). Mechanisms of control of the free Ca^{2+} concentration in the endoplasmic reticulum of mouse pancreatic β-cells: interplay with cell metabolism and $[Ca^{2+}]_c$ and role of SERCA2b and SERCA3. *Diabetes* **60**, 2533-2545. doi:10.2337/db10-1543

Rieusset, J. (2018). The role of endoplasmic reticulum-mitochondria contact sites in the control of glucose homeostasis: an update. *Cell Death Dis.* **9**, 388. doi:10.1038/s41419-018-0416-1

Roe, M. W., Mertz, R. J., Lancaster, M. E., Worley, J. F. and Dukes, I. D. (1994). Thapsigargin inhibits the glucose-induced decrease of intracellular Ca^{2+} in mouse islets of Langerhans. *Am. J. Physiol. Endocrinol. Metab.* **266**, E852-E862. doi:10.1152/ajpendo.1994.266.6.e852

Rorsman, P. and Ashcroft, F. M. (2018). Pancreatic β-cell electrical activity and insulin secretion: of mice and men. *Physiol. Rev.* **98**, 117-214. doi:10.1152/physrev.00008.2017

Rosivatz, E. and Woscholski, R. (2011). Removal or masking of phosphatidylinositol(4,5)bisphosphate from the outer mitochondrial membrane causes mitochondrial fragmentation. *Cell. Signal.* **23**, 478-486. doi:10.1016/j.cellsig.2010.10.025

Rossi, A., Pizzo, P. and Filadi, R. (2019). Calcium, mitochondria and cell metabolism: A functional triangle in bioenergetics. *Biochim. Biophys. Acta (BBA) Mol. Cell Res.* **1866**, 1068-1078. doi:10.1016/j.bbamcr.2018.10.016

Saheki, Y. and De Camilli, P. (2017). Endoplasmic reticulum-plasma membrane contact sites. *Annu. Rev. Biochem.* **86**, 659-684. doi:10.1146/annurev-biochem-061516-044932

Schindelin, J., Arganda-Carreras, I., Frise, E., Kaynig, V., Longair, M., Pietzsch, T., Preibisch, S., Rueden, C., Saalfeld, S., Schmid, B. et al. (2012). Fiji: an open-source platform for biological-image analysis. *Nat. Methods* **9**, 676-682. doi:10.1038/nmeth.2019

Suh, B.-C., Leal, K. and Hille, B. (2010). Modulation of high-voltage activated Ca2+ channels by membrane phosphatidylinositol 4,5-bisphosphate. *Neuron* **67**, 224-238. doi:10.1016/j.neuron.2010.07.001

Sun, E. W., Guillén-Samander, A., Bian, X., Wu, Y., Cai, Y., Messa, M. and De Camilli, P. (2019). Lipid transporter TMEM24/C2CD2L is a Ca^{2+} -regulated component of ER–plasma membrane contacts in mammalian neurons. *Proc. Natl. Acad. Sci. USA* **116**, 5775-5784. doi:10.1073/pnas.1820156116

Tu, H., Nelson, O., Bezprozvanny, A., Wang, Z., Lee, S.-F., Hao, Y.-H., Serneels, L., De Strooper, B., Yu, G. and Bezprozvanny, I. (2006). Presenilins form ER Ca2+ leak channels, a function disrupted by familial Alzheimer's disease-linked mutations. *Cell* **126**, 981-993. doi:10.1016/j.cell.2006.06.059

Vecellio Reane, D., Rizzuto, R. and Raffaello, A. (2020). The ER-mitochondria tether at the hub of Ca^{2+} signaling. *Curr. Opin. Physiol.* **17**, 261-268. doi:10.1016/j.cophys.2020.08.013

Vignais, P. M., Vignais, P. V. and Lehninger, A. L. (1963). Restoration of ATP-induced contraction of "aged" mitochondria by phosphatidyl inositol. *Biochem. Biophys. Res. Commun.* **11**, 313-318. doi:10.1016/0006-291X(63)90563-1

Wang, Q.-C., Zheng, Q., Tan, H., Zhang, B., Li, X., Yang, Y., Yu, J., Liu, Y., Chai, H., Wang, X. et al. (2016). TMCO1 is an ER Ca^{2+} load-activated Ca^{2+} channel. *Cell* **165**, 1454-1466. doi:10.1016/j.cell.2016.04.051

Wang, X., Wang, Q.-C., Sun, Z., Li, T., Yang, K., An, C., Guo, C. and Tang, T.-S. (2019). ER stress mediated degradation of diacylglycerol acyltransferase impairs mitochondrial functions in TMCO1 deficient cells. *Biochem. Biophys. Res. Commun.* **512**, 914-920. doi:10.1016/j.bbrc.2019.03.115

Wu, J., Prole, D. L., Shen, Y., Lin, Z., Gnanasekaran, A., Liu, Y., Chen, L., Zhou, H., Chen, S. R. W., Usachev, Y. M. et al. (2014). Red fluorescent genetically encoded Ca2+ indicators for use in mitochondria and endoplasmic reticulum. *Biochem. J.* **464**, 13-22. doi:10.1042/BJ20140931

Wuttke, A. (2015). Lipid signalling dynamics at the β-cell plasma membrane. *Basic Clin. Pharmacol. Toxicol.* **116**, 281-290. doi:10.1111/bcpt.12369

Wuttke, A., Idevall-Hagren, O. and Tengholm, A. (2013). P2Y1 receptor-dependent diacylglycerol signaling microdomains in β cells promote insulin secretion. *FASEB J.* **27**, 1610-1620. doi:10.1096/fj.12-221499

Wuttke, A., Yu, Q. and Tengholm, A. (2016). Autocrine signaling underlies fast repetitive plasma membrane translocation of conventional and novel protein kinase C isoforms in β cells. *J. Biol. Chem.* **291**, 14986-14995. doi:10.1074/jbc.M115.698456

Xie, B., Nguyen, P. M., Guček, A., Thonig, A., Barg, S. and Idevall-Hagren, O. (2016). Plasma membrane phosphatidylinositol 4,5-bisphosphate regulates Ca2+-influx and insulin secretion from pancreatic β cells. *Cell Chem. Biol.* **23**, 816-826. doi:10.1016/j.chembiol.2016.06.009

Xie, B., Nguyen, P. M. and Idevall-Hagren, O. (2019). Feedback regulation of insulin secretion by extended synaptotagmin-1. *FASEB J.* **33**, 4716-4728. doi:10.1096/fj.201801878R

Zewe, J. P., Miller, A. M., Sangappa, S., Wills, R. C., Goulden, B. D. and Hammond, G. R. V. (2020). Probing the subcellular distribution of phosphatidylinositol reveals a surprising lack at the plasma membrane. *J. Cell Biol.* **219**, e201906127. doi:10.1083/JCB.201906127

Zhao, Y., Araki, S., Wu, J., Teramoto, T., Chang, Y.-F., Nakano, M., Abdelfattah, A. S., Fujiwara, M., Ishihara, T., Nagai, T. et al. (2011). An expanded palette of genetically encoded Ca^{2+} indicators. *Science* **333**, 1888-1891. doi:10.1126/science.1208592
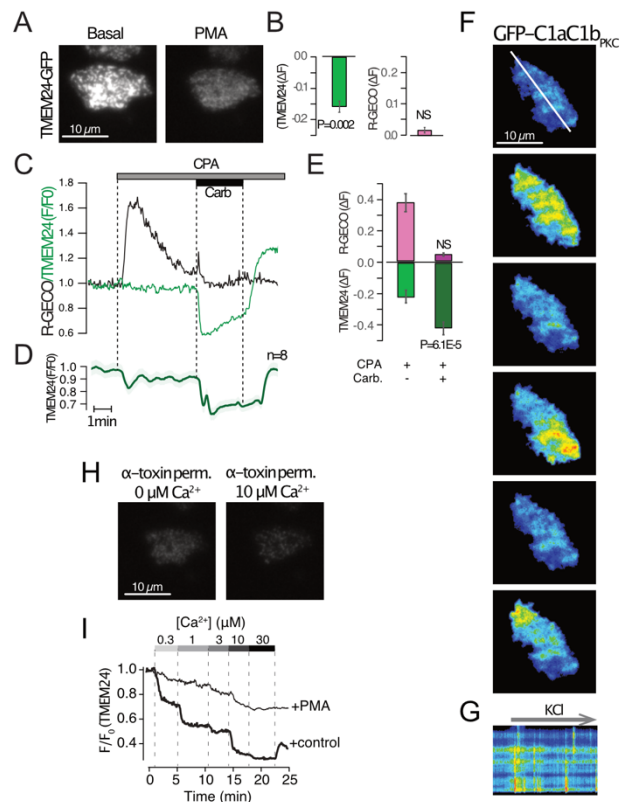
Fig. S1.

(A)   TIRF microscopy images GFP-TMEM24 fluorescence from a MIN6 cell exposed to 1 μM of the DAG analogue PMA.

(B)   Quantifications of the PMA-induced dissociation of GFP-TMEM24 from the plasma membrane and the corresponding R-GECO fluorescence change in the same cells (means±SEM for 14 cells).

(C)   TIRF microscopy recording of R-GECO (black; Ca^{2+}) and GFP-TMEM24 (green) fluorescence from a MIN6 cells exposed to 100 μM CPA and 10 μM carbachol.

(D)   Average GFP-TMEM24 fluorescence change from 6 cells on one coverslip.

(E)   Quantifications of the CPA- and charbachol-induced changes in GFP-TMEM24 plasma membrane fluorescence and the corresponding R-GECO fluorescence change in the same cells (means±SEM for 65 cells).

(F, G)   TIRF microscopy images from a MIN6 cell expressing the DAG-sensor GFP-C1aC1b$_{PKC}$
during depolarization with 30 mM KCl. Notice the irregular formation of DAG at the plasma
membrane, apparent as transient, localized fluorescence increase events in the kymograph in
D.

(H)   TIRF microscopy images GFP-TMEM24 fluorescence from an α-toxin-permeabilized MIN6
cell pre-incubated with 1 μM of the DAG analogue PMA and exposed to the indicated Ca^{2+}
buffer.

(I)   TIRF microscopy recordings of GFP-TMEM24 fluorescence from two representative α-toxin-
permeabilized MIN6 cells exposed (grey) or not (black) to 1 μM PMA. Notice that
preincubation with PMA leads to reduced Ca^{2+}-induced GFP-TMEM24 plasma membrane
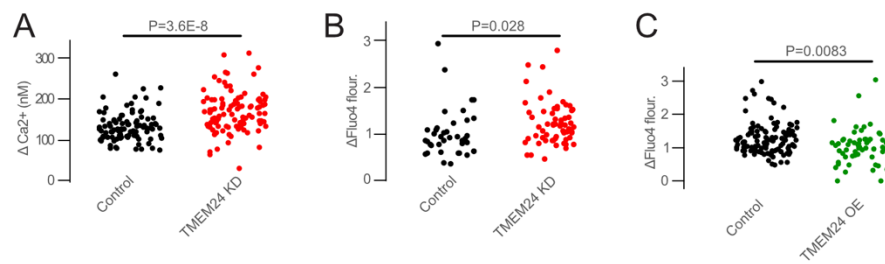dissociation.

Fig. S2.

(A) Ca^{2+} concentration change in response to 100 µM CPA in MIN6 cells treated for 48h with control siRNA (black) or siRNA against TMEM24 (red). Ca^{2+} measurements were done with Fura-2.

(B) Ca^{2+} concentration change in response to 10 µM carbachol in MIN6 cells treated for 48h with control siRNA (black) or siRNA against TMEM24 (red). Ca^{2+} measurements were done with Fluo-4.

(C) Ca^{2+} concentration change in response to 100 µM CPA in MIN6 cells over-expressing mCherry (control; black) or mCherry-TMEM24 (TMEM24 OE; green). Ca^{2+} measurements were done with Fluo-4.
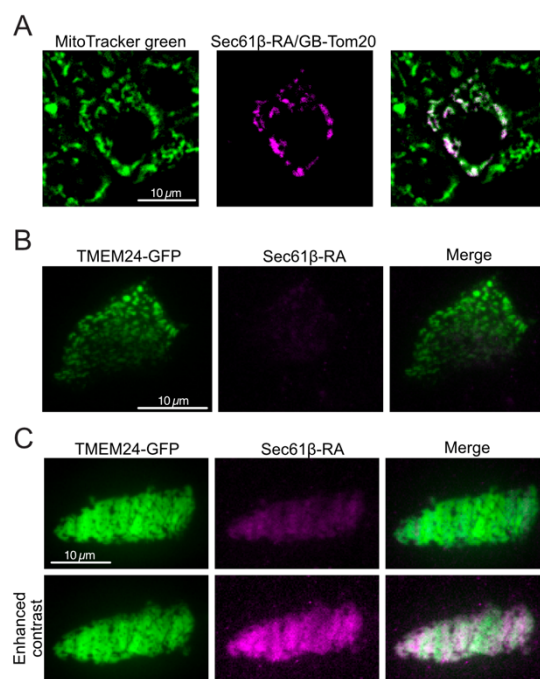
Fig. S3.

(A)   Confocal microscopy images of MIN6 cells expressing the ER-mitochondria contact site reporter (Sec61b-RA+ GB-Tom20; magenta) and loaded with MitoTracker green to label mitochondria (green).

(B)   TIRF microscopy images of a MIN6 cell expressing TMEM24-GFP (green) and Sec61b-RA. Notice the very weak fluorescence from Sec61b-RA in the absence of any GB expression.

(C)   TIRF microscopy images of a MIN6 cell expressing TMEM24-GFP (green) and Sec61b-RA. Notice that RA fluorescence is very dim in the absence of GB expression, but that contrast enhancement reveals RA fluorescence that overlaps with that of TMEM24-GFP, consistent with ER-localization.